Since January 2020 Elsevier has created a COVID-19 resource centre with free information in English and Mandarin on the novel coronavirus COVID-19. The COVID-19 resource centre is hosted on Elsevier Connect, the company's public news and information website.

Cell Reports

Article

Systematic analysis of SARS-CoV-2 infection of an ACE2-negative human airway cell

Graphical abstract

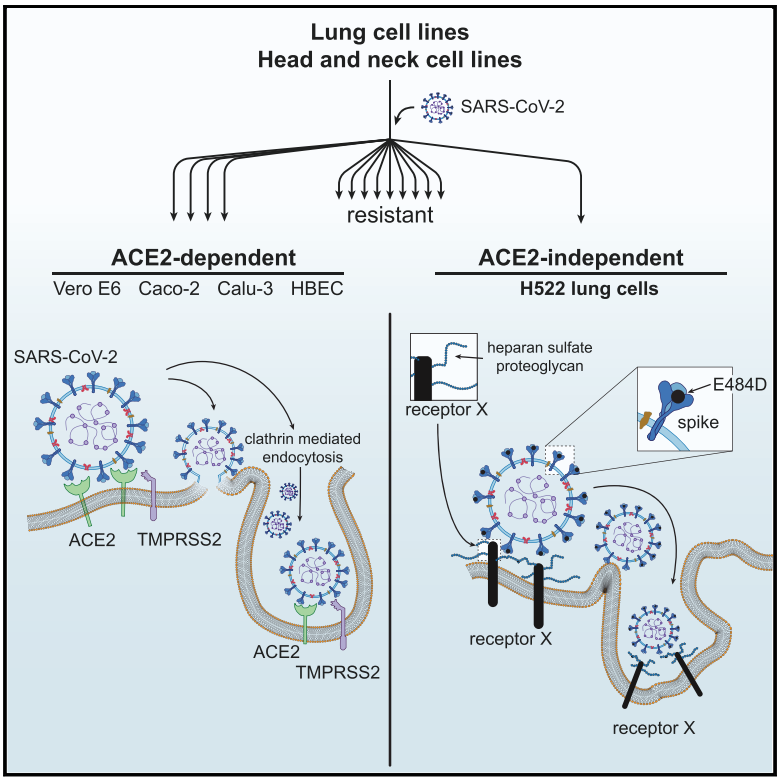

Highlights

- H522 human lung cells support SARS-CoV-2 replication independent of ACE2
- Viral entry in H522 cells requires the E484D mutation in spike
- H522 infection requires surface heparan sulfates and clathrin-mediated endocytosis
- Sera from vaccinated patients block the alternative entry pathway in H522 cells

Authors

Maritza Puray-Chavez, Kyle M. LaPak, Travis P. Schrank, ..., Dennis Goldfarb, M. Ben Major, Sebla B. Kutluay

Correspondence

bmajor@wustl.edu (M.B.M.), kutluay@wustl.edu (S.B.K.)

In brief

Variants in the SARS-CoV-2 spike enhance transmissibility and disease severity. Puray-Chavez et al. report a human lung cell line that naturally supports E484 variant SARS-CoV-2 infection independently of ACE2 expression. This alternative entry mechanism may underlie the complex COVID-19 pathogenesis and impact future therapeutic design.

Puray-Chavez et al., 2021, Cell Reports *36*, 109364
July 13, 2021
https://doi.org/10.1016/j.celrep.2021.109364

CellPress

Cell Reports

CellPress
OPEN ACCESS

Article

Systematic analysis of SARS-CoV-2 infection of an ACE2-negative human airway cell

Maritza Puray-Chavez,[1,18] Kyle M. LaPak,[2,18] Travis P. Schrank,[3,4] Jennifer L. Elliott,[1] Dhaval P. Bhatt,[2] Megan J. Agajanian,[5] Ria Jasuja,[2] Dana Q. Lawson,[1] Keanu Davis,[1] Paul W. Rothlauf,[1,6] Zhuoming Liu,[1] Heejoon Jo,[7] Nakyung Lee,[1] Kasyap Tenneti,[1] Jenna E. Eschbach,[1] Christian Shema Mugisha,[1] Emily M. Cousins,[3] Erica W. Cloer,[3] Hung R. Vuong,[1] Laura A. VanBlargan,[12] Adam L. Bailey,[8] Pavlo Gilchuk,[9] James E. Crowe, Jr.,[9,10,11] Michael S. Diamond,[1,8,12,13] D. Neil Hayes,[7] Sean P.J. Whelan,[1] Amjad Horani,[2,14] Steven L. Brody,[15] Dennis Goldfarb,[2,16] M. Ben Major,[2,17,*] and Sebla B. Kutluay[1,19,*]

[1]Department of Molecular Microbiology, Washington University in St. Louis, School of Medicine, St. Louis, MO, USA
[2]Department of Cell Biology and Physiology, Washington University in St. Louis, School of Medicine, St. Louis, MO, USA
[3]Lineberger Comprehensive Cancer Center, University of North Carolina at Chapel Hill School of Medicine, Chapel Hill, NC, USA
[4]Department of Otolaryngology/Head and Neck Surgery, University of North Carolina at Chapel Hill School of Medicine, Chapel Hill, NC, USA
[5]Department of Pharmacology, University of North Carolina at Chapel Hill, Chapel Hill, NC, USA
[6]Program in Virology, Harvard Medical School, Boston, MA, USA
[7]University of Tennessee Health Science Center for Cancer Research, Department of Medicine, Division of Hematology and Oncology, University of Tennessee, Memphis, TN, USA
[8]Department of Pathology & Immunology, Washington University in St. Louis, School of Medicine, St. Louis, MO, USA
[9]Vanderbilt Vaccine Center, Vanderbilt University Medical Center, Nashville, TN 37232, USA
[10]Department of Pediatrics, Vanderbilt University Medical Center, Nashville, TN 37232, USA
[11]Department of Pathology, Microbiology, and Immunology, Vanderbilt University Medical Center, Nashville, TN 37232, USA
[12]Department of Medicine, Washington University in St. Louis, School of Medicine, St. Louis, MO 63110, USA
[13]The Andrew M. and Jane M. Bursky Center for Human Immunology and Immunotherapy Programs, Washington University School of Medicine, St. Louis, St. Louis, MO 63110, USA
[14]Department of Pediatrics, Washington University in St. Louis, School of Medicine, St. Louis, MO, USA
[15]Division of Pulmonary and Critical Care Medicine, Department of Medicine, Washington University in St. Louis, School of Medicine, St. Louis, MO, USA
[16]Institute for Informatics, Washington University in St. Louis, School of Medicine, St. Louis, MO, USA
[17]Department of Otolaryngology, Washington University in St. Louis, School of Medicine, St. Louis, MO, USA
[18]These authors contributed equally
[19]Lead contact
*Correspondence: bmajor@wustl.edu (M.B.M.), kutluay@wustl.edu (S.B.K.)
https://doi.org/10.1016/j.celrep.2021.109364

SUMMARY

Severe acute respiratory syndrome coronavirus 2 (SARS-CoV-2) spike (S) variants govern transmissibility, responsiveness to vaccination, and disease severity. In a screen for new models of SARS-CoV-2 infection, we identify human H522 lung adenocarcinoma cells as naturally permissive to SARS-CoV-2 infection despite complete absence of angiotensin-converting enzyme 2 (ACE2) expression. Remarkably, H522 infection requires the E484D S variant; viruses expressing wild-type S are not infectious. Anti-S monoclonal antibodies differentially neutralize SARS-CoV-2 E484D S in H522 cells as compared to ACE2-expressing cells. Sera from vaccinated individuals block this alternative entry mechanism, whereas convalescent sera are less effective. Although the H522 receptor remains unknown, depletion of surface heparan sulfates block H522 infection. Temporally resolved transcriptomic and proteomic profiling reveal alterations in cell cycle and the antiviral host cell response, including MDA5-dependent activation of type I interferon signaling. These findings establish an alternative SARS-CoV-2 host cell receptor for the E484D SARS-CoV-2 variant, which may impact tropism of SARS-CoV-2 and consequently human disease pathogenesis.

INTRODUCTION

Severe acute respiratory syndrome coronavirus 2 (SARS-CoV-2) is the causative agent of the ongoing coronavirus disease 2019 (COVID-19) pandemic (Wu et al., 2020; Zhou et al., 2020). Severe COVID-19 is marked by virus-induced lung damage (Wu and McGoogan, 2020), elevated levels of pro-inflammatory cytokines, immune cell infiltration in the lung (Chen et al., 2020; Huang et al., 2020), and multi-system involvement (Varga et al., 2020). The emergence of new SARS-CoV-2 variants bearing mutations in the viral spike (S) protein and recent reports of alternative viral entry mechanisms (Cantuti-Castelvetri et al., 2020;

Clausen et al., 2020; Daly et al., 2020; Wang et al., 2021) demand comprehensive understanding of viral entry, replication, and the host cell response. This knowledge will empower new therapeutics and vaccines to thwart future viral outbreaks.

SARS-CoV-2 homotrimeric viral S protein binding to the host cell angiotensin-converting enzyme 2 (ACE2) receptor mediates viral entry (Hoffmann et al., 2020; Letko et al., 2020; Walls et al., 2020; Zhou et al., 2020). Although ACE2 is present throughout the respiratory tract (Hou et al., 2020), its expression is relatively low (Aguiar et al., 2020; Hikmet et al., 2020) compared to the gastrointestinal tract, kidney, and myocardium (Hamming et al., 2004; Qi et al., 2020; Sungnak et al., 2020; To and Lo, 2004; Zhao et al., 2020; Zou et al., 2020). Low levels of ACE2 expression may be compensated by additional attachment/entry factors. For example, recent studies revealed that neuropilin-1 (NRP1) and heparan sulfate facilitate ACE2-dependent SARS-CoV-2 entry *in vitro* (Cantuti-Castelvetri et al., 2020; Clausen et al., 2020; Daly et al., 2020). Additionally, the tyrosine-protein kinase receptor AXL promotes SARS-CoV-2 S pseudotyped lentivirus entry in an ACE2-independent manner; however, AXL expression has less impact on the entry and the replication of fully infectious SARS-CoV-2 entry (Wang et al., 2021). Finally, immune receptors, such as CLR, L-SIGN, and DC-SIGN are implicated in SARS-CoV-2 entry, which may contribute to virus-induced proinflammatory responses (Amraie et al., 2020; Gao et al., 2020).

SARS-CoV-2 primarily infects ciliated and type 2 pneumocyte cells in the human lung (Schaefer et al., 2020). As such, differentiated primary airway epithelial cells represent one of the most physiologically relevant models to study SARS-CoV-2 infection in culture. However, these cells require culture at an air-liquid interface, complex media formulations, and weeks of differentiation. Multiple cell lines are routinely used to study betacoronavirus infection. African green monkey kidney Vero cells are commonly used to propagate and study SARS-CoV-2 (Cagno, 2020; Chu et al., 2020b). The exceptional permissiveness of Vero cells is likely due to an ablated type I interferon (IFN) gene locus (Desmyter et al., 1968; Diaz et al., 1988; Osada et al., 2014). The lack of a type I IFN response and the presence of species-specific host responses to viral pathogens (Long et al., 2019; Malim and Bieniasz, 2012; Rothenburg and Brennan, 2020) limit the utility and physiological relevance of Vero cell infection experiments. Although human Caco-2 colorectal adenocarcinoma and Huh-7 hepatocellular carcinoma cell lines support SARS-CoV-2 replication in an ACE2-dependent manner (Chu et al., 2020b; Kim et al., 2020; Ou et al., 2020), the only human lung cell line widely reported to be permissive to SARS-CoV-2 replication is Calu-3, albeit with lower infectivity compared to Vero cells (Chu et al., 2020b; Ou et al., 2020). The general lack of permissiveness to SARS-CoV-2 infection in lung-derived cell lines is rescued by ectopic overexpression of the ACE2 receptor, suggesting that viral entry constitutes a principal block to virus replication (Blanco-Melo et al., 2020).

In addition to ACE2 expression, cellular tropism of SARS-CoV-2 may be determined by cell-intrinsic and innate immune defenses. Recognition of viral replication intermediates, typically viral nucleic acids, by Toll-like receptors (TLRs) and RIG-I-like receptors (RLRs) culminate in secretion of type I and type III IFNs (Lazear et al., 2019; Schoggins, 2018). Type I/III IFN signaling results in the upregulation of numerous IFN-stimulated genes (ISGs), which collectively establish an antiviral state. SARS-CoV-2 induces lower levels of type I/III IFNs *in vitro* compared with other respiratory pathogens (Blanco-Melo et al., 2020; Chu et al., 2020a; Stukalov et al., 2020), possibly due to the actions of SARS-CoV-2 proteins, including Nsp1 and ORF6 (Xia et al., 2020). Type I IFN pretreatment of cell culture models potently suppresses SARS-CoV-2 replication (Lokugamage et al., 2020; Xie et al., 2020), suggesting a potentially important role of this pathway in defining cellular tropism.

To identify new lung and upper airway cell culture models that are naturally permissive to SARS-CoV-2 infection, we infected a panel of human lung and head/neck cancer cell lines expressing varying levels of ACE2 and the TMPRSS2 protease. Unexpectedly, we found that the H522 lung adenocarcinoma cell line, which does not express detectable levels of ACE2 or TMPRSS2, supports efficient SARS-CoV-2 replication. Infection of H522 cells is independent of ACE2 expression, requires the viral S protein, and is suppressed by endosomal cathepsin function. We further found that infection is independent of other reported alternative receptors, including AXL and NRP1, but is dependent on surface heparan sulfates. Strikingly, the E484D substitution within the receptor-binding domain (RBD) of S is required for H522 infection. Monoclonal antibodies targeting the N-terminal domain of S specifically neutralized SARS-CoV-2 replication in H522 cells, but not Vero cells, highlighting the differential usage of S for entry into H522 cells. Sera from vaccine recipients potently blocked this alternative entry mechanism, whereas convalescent sera were less effective. Time-resolved transcriptomic and proteomic profiling of SARS-CoV-2-infected H522 cells identified a robust activation of type I IFN responses in a MDA5-dependent manner, activation of clathrin-mediated endocytosis (CME), and modulation of cell cycle-associated genes and pathways. Chemical inhibition of the AAK1 kinase, which potentiates CME, suppressed SARS-CoV-2 infection of H522 cells as well as primary human airway cultures. The ACE2- and TMPRSS2-independent infection of H522 cells establishes the presence of an alternative entry pathway for SARS-CoV-2 in human airway cells. Comprehensive understanding of these entry mechanisms may better explain the complex COVID-19 disease pathogenesis and aid in the design of new and effective therapies.

RESULTS

H522 human lung adenocarcinoma cells are permissive to SARS-CoV-2 infection

To identify additional cell types to model SARS-CoV-2 infection, we performed RNA sequencing (RNA-seq) analysis on a panel of 10 lung and head/neck cancer cell lines, revealing varied expression levels of *ACE2* and *TMPRSS2* as well as other entry factors, including proteases involved in S cleavage (*FURIN, CTSB*, *CTSL*) and *NRP1* (Cantuti-Castelvetri et al., 2020; Daly et al., 2020) (Figures 1A and S1; Table S1). Normalized RNA-seq read counts for established SARS-CoV-2 cell models Caco-2, Calu-3, and Vero E6 enabled comparative analysis (Figures 1A and S1; Table S1). Validation by qRT-PCR and protein quantification by immunoblotting showed ACE2 protein levels ranging from undetectable to 2- to 3-fold lower than Vero E6 cells, currently one of the most

CellPress
OPEN ACCESS

A

Gene	Colon	Lung		Lung						Head/Neck			
	Caco-2	Calu-3	Vero E6	H522	H596	H1299	A427	HCC827	PC-9	Detroit562	SCC25	OE21	KYSE30
ACE2	6.99	8.22	2.01	0	5.74	0.46	0	1.89	2.84	5.44	4.64	3.32	0.60
TMPRSS2	9.74	6.63	0.00	0	2.89	0	0	1.78	0.98	6.99	0	1.29	0
FURIN	9.97	9.63	6.70	8.88	9.50	10.07	9.33	8.60	10.05	9.14	11.28	10.24	10.64
CTSB	12.25	11.30	3.94	10.65	11.21	11.69	11.08	10.67	10.97	12.87	12.94	12.08	11.02
CTSL	10.06	8.56	8.94	8.91	10.14	10.58	9.29	9.68	9.76	8.68	11.74	11.10	8.85
NRP1	10.43	10.58	3.08	3.10	11.33	7.43	0.21	11.97	9.83	8.20	11.14	10.54	9.89

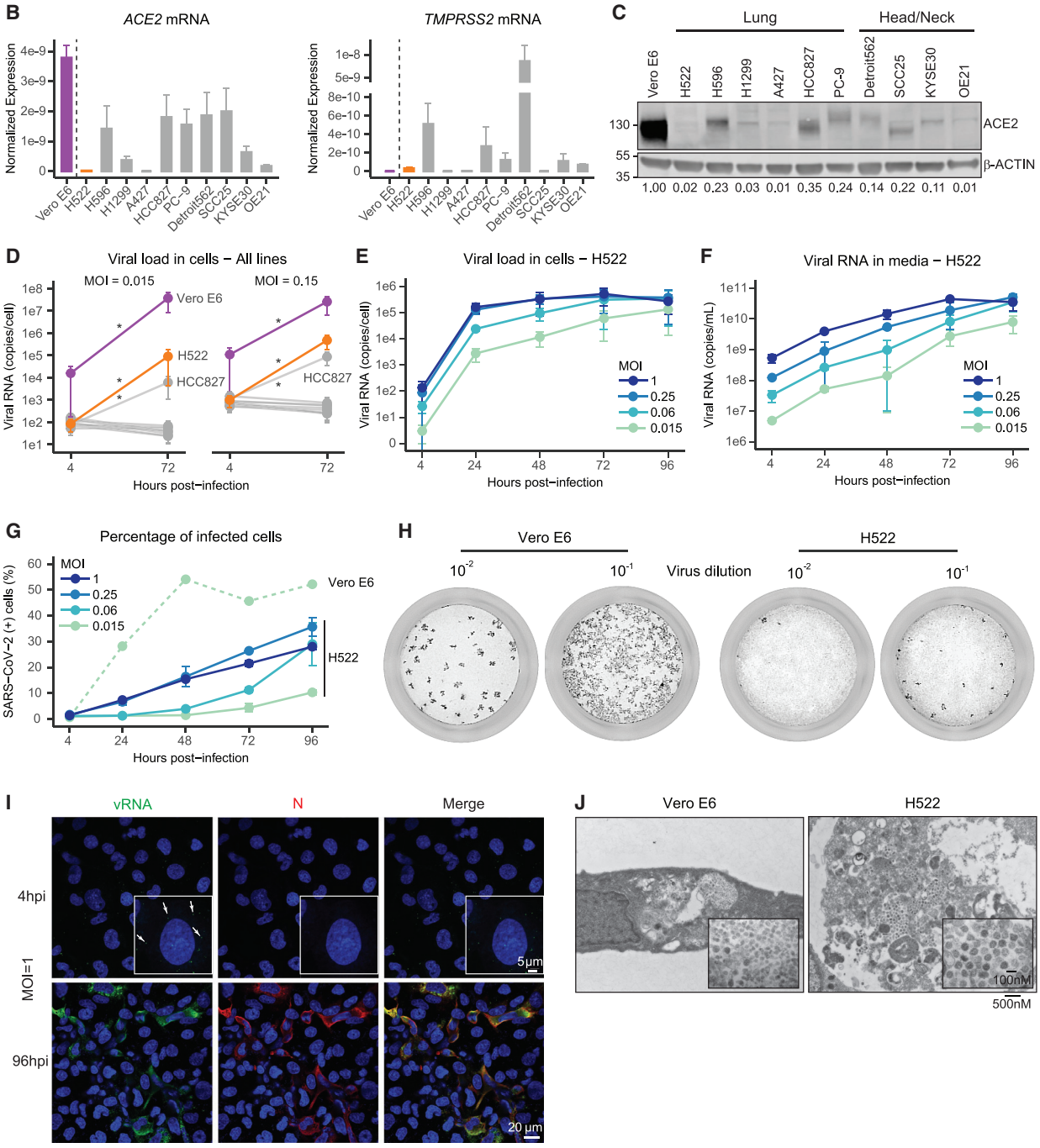

(legend on next page)

permissive cell models for SARS-CoV-2 infection (Figures 1B and 1C). The observed cell line-dependent differences in ACE2 protein migration are possibly due to post-translational modifications, including glycosylation (Figure 1C) (Shajahan et al., 2021; Walls et al., 2020; Wrapp et al., 2020; Yang et al., 2020). Each cell line then was inoculated with SARS-CoV-2 before quantification of cell-associated viral RNA (vRNA) at 4 and 72 h post-infection (hpi) (Figure 1D). Most cell lines, including those expressing ACE2 and TMPRSS2 at relatively high levels (i.e., Detroit562 and H596), were not permissive to SARS-CoV-2 replication (Figure 1D). H522 cells, and to a lesser degree HCC827 cells, supported virus replication (Figure 1D). Unexpectedly, neither ACE2 nor TMPRSS2 was detected in H522 cells (Figures 1A–1D).

Given the possibility of ACE2-independent infection, we focused our efforts on H522 cells. To define viral replication kinetics, H522 cells were inoculated at various multiplicities of infection (MOIs) before monitoring for virus growth over 4 days. Cell-associated viral RNA levels increased substantially (3–4 $\log_{10}$) within 24 h of infection in an MOI-responsive manner (Figure 1E) and corresponded to elevated viral RNA levels in the cell culture supernatants (Figure 1F). We confirmed replication competency of virus released from H522 cells through plaque assays on Vero cells (up to 2.2×10^5 plaque-forming units [PFU]/mL, data not shown). Although permissive, infection progressed slower in H522 cells than in Vero E6 cells, and higher doses of the virus were required to achieve similar percentages of infected cells (Figure 1G). Viruses formed plaques on H522 cells, and plaque sizes were comparable to those obtained on Vero E6 cells, albeit the effective MOI was ~20-fold lower (Figure 1H).

Quantified RNA *in situ* hybridization (ISH) revealed the kinetics of SARS-CoV-2 viral replication and spread in H522 cells (Figures 1I, S2A, and S2B). Incoming virions were readily detected at 4 hpi in cells infected with an MOI of 1 (white arrows to green puncta; Figure 1I). As expected, both the number of cells positive for viral RNA and the number of viral RNA puncta/cell were MOI-dependent (Figures S2A and S2B). We tracked viral spread over time and observed increased staining for both viral RNA and N, and an increased number of infected cells per field (Figure S2A). Furthermore, similar to Vero cells, virions were observed in membrane-limited compartments in infected H522 cells and frequently in apoptotic cells (Figure 1J). These results show that H522 cells are productively infected with SARS-CoV-2 despite lacking detectable levels of ACE2/TMPRSS2 expression.

Infection of H522 cells depends on SARS-CoV-2 S and requires the E484D substitution

SARS-CoV-2 entry into host cells requires viral S-mediated engagement of the ACE2 receptor and priming of S by TMPRSS2 or other host cell proteases (Hoffmann et al., 2020; Letko et al., 2020; Walls et al., 2020; Zhou et al., 2020). Because ACE2 and TMPRSS2 mRNA and protein were not detected in H522 cells (Figures 1A–1C), we tested the dependency on S for SARS-CoV-2 infection. H522 parental cells, H522 cells stably expressing ACE2 (H522-ACE2), and Vero E6 cells were infected with SARS-CoV-2 in the presence of a S neutralizing antibody (Alsoussi et al., 2020) or soluble human ACE2-Fc decoy receptor (Figures 2A–2C) (Case et al., 2020). Blockade of S significantly diminished the amount of cell-associated viral RNA in H522, H522-ACE2, and Vero E6 cells (Figures 2B and 2C). The decreased sensitivity of H522-ACE2 cells to treatment as compared to parental H522 cells likely reflects the high overexpression of ACE2 (Figure 2A).

We next investigated whether S is sufficient for viral entry in H522 cells. For this, we used a replication-competent GFP reporter vesicular stomatitis virus (VSV) that expresses a modified form of the SARS-CoV-2 S protein (designated VSV-GFP-SARS-CoV-2-$S_{\Delta 21}$) (Case et al., 2020). We inoculated the following cells with VSV-GFP-SARS-CoV-2-$S_{\Delta 21}$: Vero E6, H522, H522-ACE2, primary basal human bronchial epithelial cells (HBECs), and HBECs engineered to express ACE2 (basal HBEC-ACE2; Figure 2A). Whereas Vero E6, H522-ACE2, and basal-HBEC-ACE2 cells were readily infected, H522 and parental HBECs were resistant to infection by VSV-GFP-SARS-CoV-2-$S_{\Delta 21}$ (Figure 2D).

The inability of VSV-GFP-SARS-CoV-2-$S_{\Delta 21}$ to infect H522 cells prompted us to analyze sequence variation within S in our virus stocks and in infected H522 cells. This revealed the presence of the E484D substitution within the RBD and the less prevalent R682W substitution within the furin cleavage site. No other S mutations were observed. Unexpectedly, we found that virus

Figure 1. The H522 cell line is null for ACE2 expression and is permissive to SARS-CoV-2 infection

(A) Normalized RNA-seq-derived read counts for *ACE2*, *TMPRSS2*, *FURIN*, *CTSB*, *CTSL*, and *NRP1* are given for the indicated cell lines. See also Figure S1 and Table S1.

(B qRT-PCR expression normalized to 1 μg of input RNA for each cell line. Each bar represents mean; error bars indicate SEM (n = 3).

(C) ACE2 immunoblot across 10 lung and head/neck cancer cell lines and Vero E6 cells (representative of n = 3). Relative ACE2 expression levels are indicated below the immunoblots.

(D) qRT-PCR for cell-associated SARS-CoV-2 RNA at 4 and 72 hpi at an MOI of 0.015 or 0.15 (based on Vero titers). Error bars represent SEM (n = 3). *$p < 0.05$ using a two-way ANOVA test and the Šidák correction for multiple comparisons.

(E) qRT-PCR for cell-associated SARS-CoV-2 RNA (viral RNA [vRNA]) in H522 cells across various time points and MOIs. Error bars represent SEM (n = 2).

(F) qRT-PCR for SARS-CoV-2 RNA in the supernatant of H522 cells across various time points and MOIs. Error bars represent SEM (n = 2).

(G) Percentage of SARS-CoV-2-infected H522 and Vero E6 cells determined by fluorescence-activated cell sorting (FACS) for nucleocapsid (N)-positive cells across various time points and MOIs. Error bars represent SEM (n = 2).

(H) Plaque assays on H522 and Vero cells using two viral dilutions (10^{-2} and 10^{-1}). Data are representative of n = 3 experiments.

(I) Representative images of H522 cells infected with SARS-CoV-2 at an MOI of 1. H522 cells were fixed and stained for SARS-CoV-2 RNA (green) and N protein (red) at 4 and 96 hpi and imaged by confocal microscopy (representative of n = 2). See also Figure S2.

(J) Representative images using transmission electron microscopy (TEM) on Vero E6 and H522 cells infected with SARS-CoV-2 (MOI of 0.1 PFU/cell and 24 hpi for Vero, MOI of 1 PFU/cell and 96 hpi for H522).

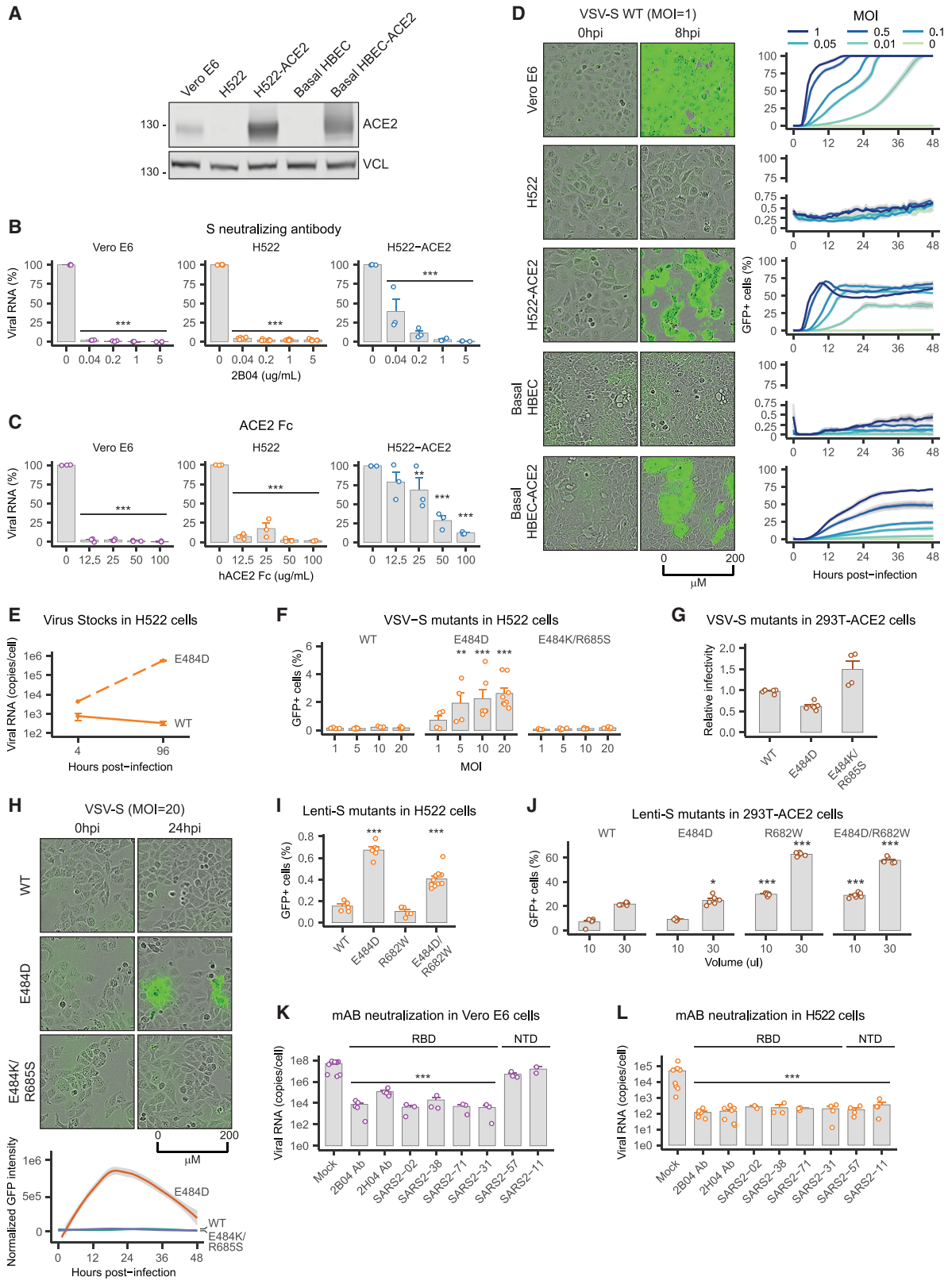

(legend on next page)

stocks containing sequence-validated wild-type (WT) S were unable to infect H522 cells (Figure 2E). We next tested the contribution of S mutations to H522 infection using chimeric VSV-GFP-SARS-CoV-2-$S_{\Delta 21}$ and lentiviral pseudoparticles. Chimeric VSV-GFP-SARS-CoV-2-$S_{\Delta 21}$ bearing the E484D substitution specifically enhanced viral entry in H522 cells but did not affect the infection of 293T-ACE2 cells (Figures 2F–2H). In contrast, E484K/R685S substitutions did not enable VSV-GFP entry into H522 cells (Figures 2F and 2H). Despite the enhanced viral entry, we observed no viral spread with VSV-GFP-SARS-CoV-2-$S_{\Delta 21}$ E484D in H522s (Figure 2H), suggesting that additional viral factors may be needed to facilitate viral egress and spread. Consistent with these findings, we found that lentivirus pseudoparticles bearing the E484D substitution allowed low but reproducibly detectable levels of infection, whereas pseudoparticles bearing WT or R682W S were unable to infect H522s (Figure 2I). Combination of the E484D and R682W substitutions did not further promote viral entry (Figure 2I). In contrast, WT and E484D lentivirus pseudoparticles efficiently infected 293T-ACE2 cells, and the R682W substitution further enhanced entry (Figure 2J).

Given the requirement for S E484D in H522 but not in ACE2-expressing cells, we screened a panel of eight S monoclonal antibodies (mAbs) in H522 and Vero E6 cells (Figures 2K and 2L). All six mAbs recognizing the S RBD domain neutralized infection of Vero E6 cells; mAbs SARS2-57 and SARS2-11, which bind the N-terminal domain (NTD) of S (Table S2), did not affect infection (Figure 2K). Remarkably, all eight mAbs blocked infection of H522 cells, demonstrating differential usage of S for the alternative entry pathway in H522 cells (Figure 2L). Taken together, these data show that S is necessary for infection of H522 cells but not sufficient. Moreover, the E484D mutation within the RBD of S is required in H522 cells, but not ACE2-expressing cells.

SARS-CoV-2 replication in H522 cells is independent of ACE2

Two orthogonal approaches were used to test whether ACE2 mediated SARS-CoV-2 infection of H522 cells. First, cells were pre-treated with anti-ACE2 blocking antibody before the addition of SARS-CoV-2. Anti-DC-SIGN and anti-GFP antibodies served as negative controls as well as the use of Chinese hamster ovary (CHO)-derived PgsA-745 cells, which are not permissive to infection (Figure 3A). While the anti-ACE2 blocking antibody significantly decreased the amount of cell-associated viral RNA in Calu-3 cells, it did not affect SARS-CoV-2 RNA levels in H522 cells (Figure 3A). As expected, neither the anti-DC-SIGN nor the anti-GFP antibodies affected viral RNA levels in H522 and Calu-3 cells, and virus replication remained at background levels in PgsA-745 cells.

In a second approach to test ACE2 involvement, we inactivated the ACE2 genetic locus by CRISPR gene editing in H522 and Calu-3 cells. Polyclonal cell populations containing CRISPR-edited loci were inoculated with SARS-CoV-2, and viral replication was monitored at 4 and 72 hpi (Figures 3B and S3A). While viral RNA levels increased at similar levels in H522 and H522 ACE2$^{-/-}$ cells, the lack of ACE2 expression significantly reduced SARS-CoV-2 replication in Calu-3 cells (Figure 3B). Moreover, the addition of an ACE2 blocking antibody did not impair virus replication in H522 or H522 ACE2$^{-/-}$ cells, but it completely abolished replication in Calu-3 cells (Figure 3C). We next isolated monoclonal cell populations of H522 ACE2 WT (n = 6), H522 ACE2$^{-/-}$ (n = 2), and H522 ACE2$^{+/-}$ (n = 1) cells to corroborate these findings (Figure S3B). Sanger sequencing of the edited loci revealed unique 5-bp deletions in exon 3 of ACE2, resulting in a truncated ACE2 protein lacking the C-terminal 672 aa (Figure S3B). SARS-CoV-2 infection of monoclonal cell lines from H522 control and H522 ACE2$^{-/-}$ resulted in similar levels of infection (Figure 3D).

We next tested the involvement of published alternative SARS-CoV-2 receptors NRP1, AXL, and heparan sulfate. Depletion of NRP1 and AXL by small interfering RNAs (siRNAs) and CRISPR did not diminish SARS-CoV-2 replication in H522 cells (Figures 3E and S3C–S3E). In contrast, removal of surface heparan sulfates by propagation of H522 cells in sodium chlorate or heparinase treatment substantially reduced virus replication (Figures 3F and 3G). Taken together, these data establish that

Figure 2. The SARS-CoV-2 S protein is necessary for viral entry in H522 cells, and the E484D mutation enhances infection

(A) Representative immunoblot showing ACE2 expression and vinculin as the loading control in Vero E6, H522, H522-ACE2, basal HBEC, and basal HBEC-ACE2 cells.
(B) SARS-CoV-2 (MOI of 0.1 equivalent) was pre-treated with increasing concentrations of S mAb (2B04) for 1 h and used to infect cells in the presence of the mAb. Cell-associated SARS-CoV-2 RNA was detected by qRT-PCR at 24 hpi and was normalized to mock-treated cells (n = 3).
(C) SARS-CoV-2 was pre-treated with increasing amounts of ACE2-Fc for 1 h as in (A) and used to infect cells in the presence of ACE2-Fc. Cell-associated SARS-CoV-2 RNA was detected by qRT-PCR at 24 hpi and was normalized to mock-treated cells (n = 3).
(D) Representative images of cells infected with VSV-SARS-CoV-2-$S_{\Delta 21}$ at 0 and 8 hpi (n = 3). Percentages of GFP-positive cells seeded in triplicate were quantified over time, with the shaded gray region indicating SD.
(E) Quantification of vRNA in H522 cells infected with WT SARS-CoV-2 and SARS-CoV-2 containing the E484D S substitution.
(F) Percentage of GFP-positive H522 cells quantified by FACS upon infection (24 hpi) with increasing MOIs of VSV-SARS-CoV-2-$S_{\Delta 21}$ containing the indicated S variants.
(G) Relative titers of VSV-SARS-CoV-2-$S_{\Delta 21}$ bearing the indicated S variants on HEK293T-ACE2 cells (6 hpi). Titers were normalized relative to WT after quantification by FACS.
(H) Representative images of H522 cells infected with the indicated variants of VSV-SARS-CoV-2-$S_{\Delta 21}$ at 0 and 24 hpi. GFP intensity was assessed as in (D).
(I) Percentage of GFP-positive cells upon infection (48 hpi) of H522 cells with 150 μL (MOI of 15–30 IU/cell) of lentiviral pseudoparticles containing the indicated S variants.
(J) Percentage of GFP-positive cells upon infection (48 hpi) of HEK293T-ACE2 cells, with the indicated volumes of lentiviral pseudoparticles bearing the indicated S variants.
(K and L) SARS-CoV-2 (MOI of 0.1) was pre-treated with the indicated concentrations of anti-S mAbs for 1 h before inoculation of Vero E6 (K) or H522 cells (L) as in (B) (see also Table S2). Amount of cell-associated vRNA was quantified as above.
RBD, receptor-binding domain; NTD, N-terminal domain. *$p < 0.05$, **$p < 0.01$, ***$p < 0.001$ where significance was assessed by a one-way (I, K, and L) or two-way ANOVA (B, C, F, and J) and the Dunnett correction for multiple comparisons.

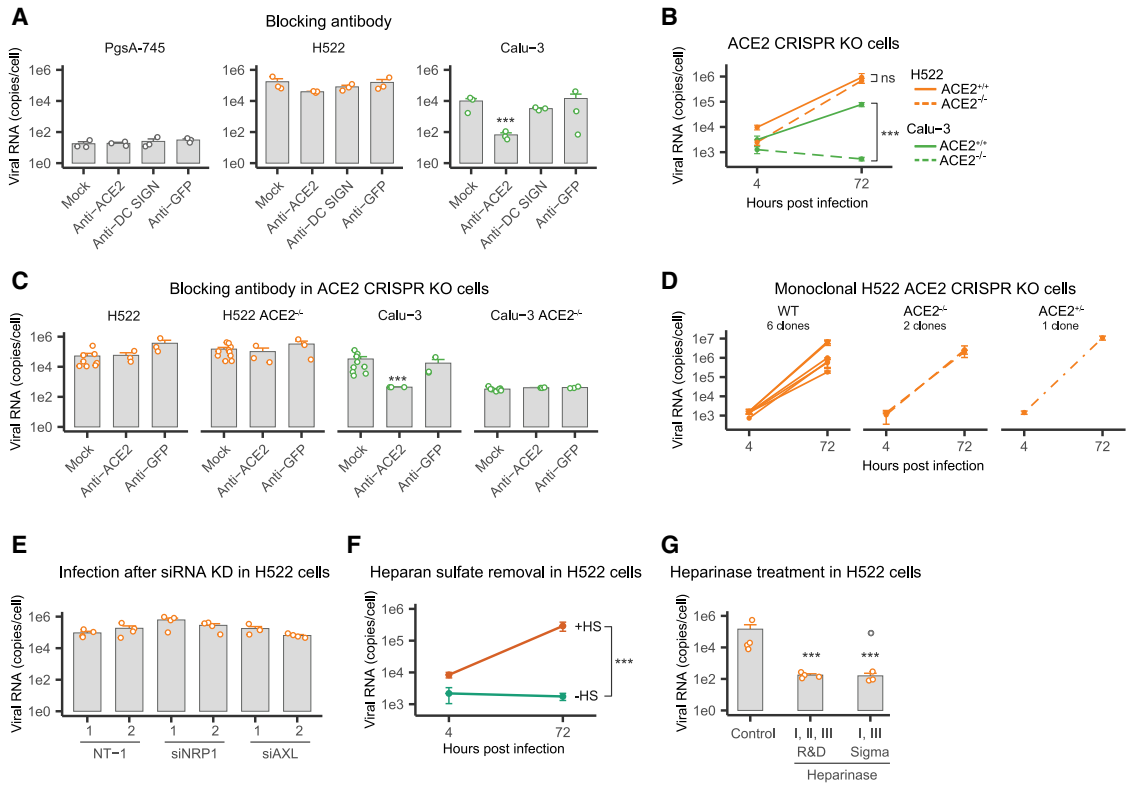

Figure 3. H522 cells are permissive to SARS-CoV-2 infection independent of ACE2 expression but require surface heparan sulfates

(A) Cells were pre-treated with 20 μg/mL of the indicated antibodies for 1 h and infected with SARS-CoV-2 at an MOI of 0.1 in the presence of antibodies. Cell-associated SARS-CoV-2 RNA was detected by qRT-PCR at 72 hpi (n = 3).

(B) Polyclonal populations of H522 and Calu-3 ($ACE2^{+/+}$ and $ACE2^{-/-}$) cells were infected with SARS-CoV-2 virus, and cell-associated SARS-CoV-2 RNA was detected by qRT-PCR at 4 and 72 hpi (n = 8). Error bars indicate the SEM. See also Figure S3.

(C) Polyclonal populations of H522 and Calu-3 ($ACE2^{+/+}$ and $ACE2^{-/-}$) cells were pre-treated with 20 μg/mL of the indicated antibodies for 1 h and then infected with SARS-CoV-2 at an MOI of 0.1 in their presence. Cell-associated SARS-CoV-2 RNA was detected by qRT-PCR at 72 hpi (n = 3). Error bars indicate the SEM. See also Figure S3.

(D) Monoclonal populations from H522 $ACE2^{+/+}$ (six clones), $ACE2^{-/-}$ (two clones), and $ACE2^{+/-}$ (one clone) were infected with SARS-CoV-2 at an MOI of 0.1, and cell-associated SARS-CoV-2 RNA was detected by qRT-PCR at 4 and 72 hpi ($n \geq 3$). Error bars indicate the SEM. See also Figure S3.

(E) H522 cells were transfected with non-targeting (NT) siRNAs or siRNAs specific against NRP1 and AXL 48 h prior to infection. Cells were infected with SARS-CoV-2 at an MOI of 1 IU/cell, and the cell-associated vRNA level assessed by qRT-PCR. See also Figure S3.

(F) H522 cells were passaged in the absence or presence of 50 mM sodium chlorate to deplete heparan sulfates before infection with SARS-CoV-2 at an MOI of 1 IU/cell. Cell-associated vRNA levels were quantitated at 4 and 72 hpi (n = 5–9).

(G) H522 cells were treated with a combination of heparinases I, II, and III from two vendors (Sigma and R&D Systems) for 90 min and then infected with SARS-CoV-2 at an MOI of 0.1 IU/cell. Cell-associated vRNA levels were quantitated at 72 hpi (n = 4). The gray dot indicates an outlier (Grubbs' method, $\alpha = 0.0001$).

***$p < 0.001$ using one-way ANOVA (G), two-way ANOVA and a Dunnett's test (A), or Tukey's correction for multiple comparisons (B, C, and F).

H522 cells are permissive to SARS-CoV-2 infection in a manner that is independent of ACE2, NRP1, and AXL, but dependent on surface heparan sulfates.

Determinants of SARS-CoV-2 infection of H522 cells

To begin to decipher the mechanism(s) of SARS-CoV-2 entry into H522 cells, we performed infections in the presence of compounds that interfere with SARS-CoV-2 entry, including camostat mesylate (TMPRSS2 inhibitor) (Hoffmann et al., 2020; Shang et al., 2020; Shema Mugisha et al., 2020a), E64D (broad spectrum inhibitor of proteases, including endosomal cathepsins) (Ou et al., 2020; Shema Mugisha et al., 2020a), bafilomycin A (inhibitor of vATPase) (Ou et al., 2020; Shema Mugisha et al., 2020a), and apilimod (inhibitor of PIKfyve) (Kang et al., 2020; Ou et al., 2020; Shema Mugisha et al., 2020a). We additionally included a specific inhibitor of AAK1 kinase (SGC-AAK1-1); AAK1 promotes CME through phosphorylation of the AP2M1 subunit of the AP2 complex (Agajanian et al., 2019; Conner and Schmid, 2002, 2003). E64D, bafilomycin A, SGC-AAK1-1, and apilimod reduced cell-associated viral RNAs in a dose-dependent manner, whereas camostat mesylate increased viral RNA levels (Figure 4A). These findings were corroborated in comparative analysis of H522, Vero E6, and H522-ACE2 cells. Bafilomycin A significantly decreased cell-associated viral RNA levels in H522 and H522-ACE2 cells but did not affect viral entry in Vero E6 cells (Figure S4). Inhibition of both AAK1 and endosomal cathepsins B/L significantly decreased viral RNA levels in H522 cells but did not impact ACE2-dependent replication at

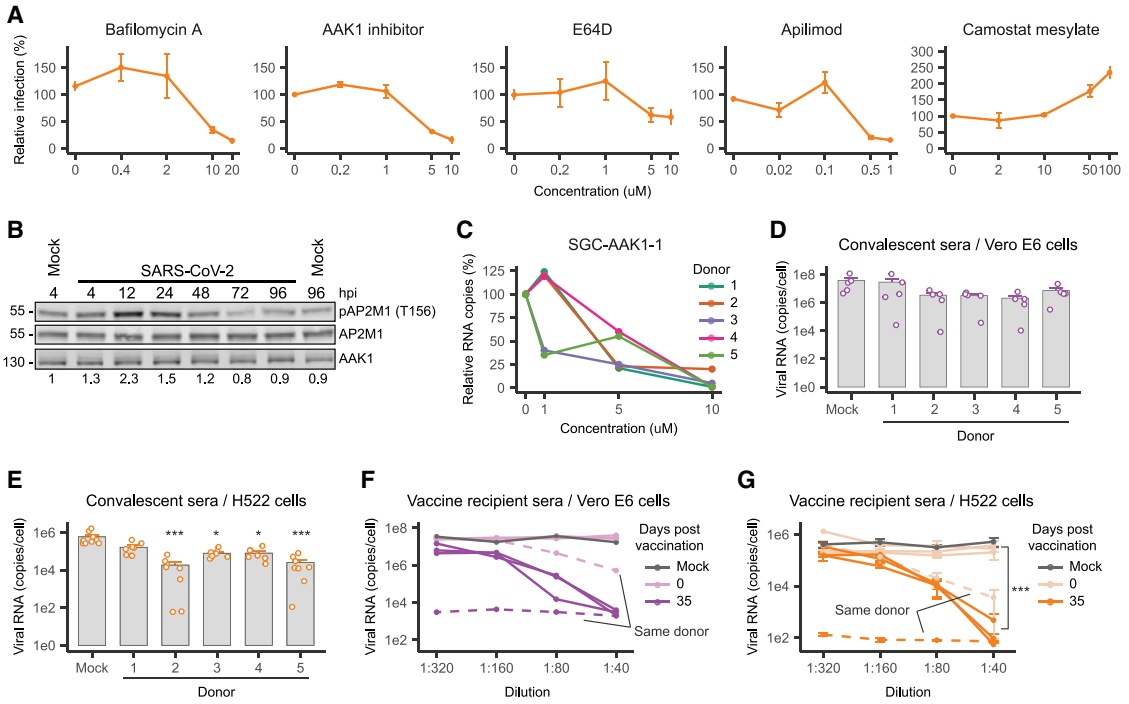

Figure 4. H522 infection by SARS-CoV-2 is dependent on clathrin-mediated endocytosis and endosomal cathepsins

(A) H522 cells were pre-treated with bafilomycin A, SGC-AAK1-1, E64D, apilimod, or camostat mesylate for 1 h and then infected with SARS-CoV-2 at an MOI of 1 in the presence of the inhibitors. Cell-associated SARS-CoV-2 RNA was detected by qRT-PCR 24 hpi and normalized to DMSO-treated cells ($n \geq 3$). See also Figure S4.

(B) Immunoblot showing pAP2M1 (T156), AP2M1, and AAK1 levels in H522 cells infected with SARS-CoV-2 (representative of n = 2). pAP2M1 (T156) levels were normalized to total AP2M1 and set relative to the 4-h mock control. Quantification is shown.

(C) Basal HBECs from five different donors were pre-treated with increasing concentrations of SGC-AAK1-1 for 2 h and then infected with SARS-CoV-2 in its presence. Cell-associated SARS-CoV-2 RNA was detected by qRT-PCR at 72 hpi and normalized to DMSO-treated cells.

(D and E) SARS-CoV-2 (MOI of 0.1 for Vero E6 and 1 IU/cell for H522) was pre-incubated with a 1:40 dilution of convalescent sera and used to infect H522 and Vero E6 cells. Cell-associated vRNA levels were analyzed at 72 hpi for H522 and 18 hpi for Vero E6 cells. *$p < 0.05$, ***$p < 0.001$ compared to mock using one-way ANOVA and Dunnett's correction for multiple comparisons.

(F and G) SARS-CoV-2 (MOI of 0.1 for Vero E6 and 1 IU/cell for H522) was pre-incubated with a 1:40 to 1:320 dilution of sera from vaccine recipients and used to infect H522 and Vero E6 cells. Cell-associated vRNA levels were analyzed at 72 hpi for H522 and 18 hpi for Vero E6 cells. ***$p < 0.001$ compared to the respective day 0 vaccinated sera at 1:40 dilution using two-way ANOVA and Tukey's correction for multiple comparisons.

appreciable levels in Vero E6 and H522-ACE2 cells at this concentration (Figure S4). While apilimod decreased viral entry in Vero E6 cells, the effect was modest in H522 cells and trended toward significance (p = 0.07; Figure S4). Finally, camostat mesylate did not decrease, but, on the contrary, increased the amount of cell-associated viral RNA in H522s, highlighting the TMPRSS2 independence of viral entry (Figure S4).

Western blot analysis of H522 cells infected with SARS-CoV-2 revealed transient induction of AP2M1 phosphorylation 12–24 hpi, further supporting the involvement of CME in H522 viral infections (Figure 4B). AAK1 inhibitors are highly specific and have been considered as therapeutic options for the treatment of SARS-CoV-2 (Richardson et al., 2020). Consistent with our observations in H522 cells, inhibition of AAK1 kinase activity in differentiated primary HBECs grown at the air-liquid interface resulted in a 10- to 20-fold decrease in cell-associated SARS-CoV-2 RNA in a dose-responsive manner (Figure 4C). Taken together, these data support a role for CME and endosomal cathepsins in SARS-CoV-2 infection of H522 cells.

The E484D S variant has been found to circulate within the human population, and given the alternative mechanism of entry and the requirement for the E484D substitution, we evaluated the ability of sera from vaccinated and convalescent individuals to block the infection of H522 cells. While sera from vaccine recipients potently neutralized SARS-CoV-2 infection of H522 and Vero E6 cells, convalescent sera were less efficient in blocking virus replication in both cell models (Figure 4D–4G).

SARS-CoV-2-infected H522 cells demonstrate RNA-level upregulation of type I IFN responses and modulation of cell cycle genes

To determine how H522 cells respond to SARS-CoV-2 infection, we conducted RNA-seq on cells infected at high and low MOIs and followed the infection during the course of 4 days (Figure 5A). As expected, SARS-CoV-2 mRNA levels increased with time and MOI, and plateaued at 24–48 hpi (Figure 5B). At the peak of infection, 5%–10% of total reads mapped to SARS-CoV-2 RNAs. Principal-component analysis (PCA) showed that samples

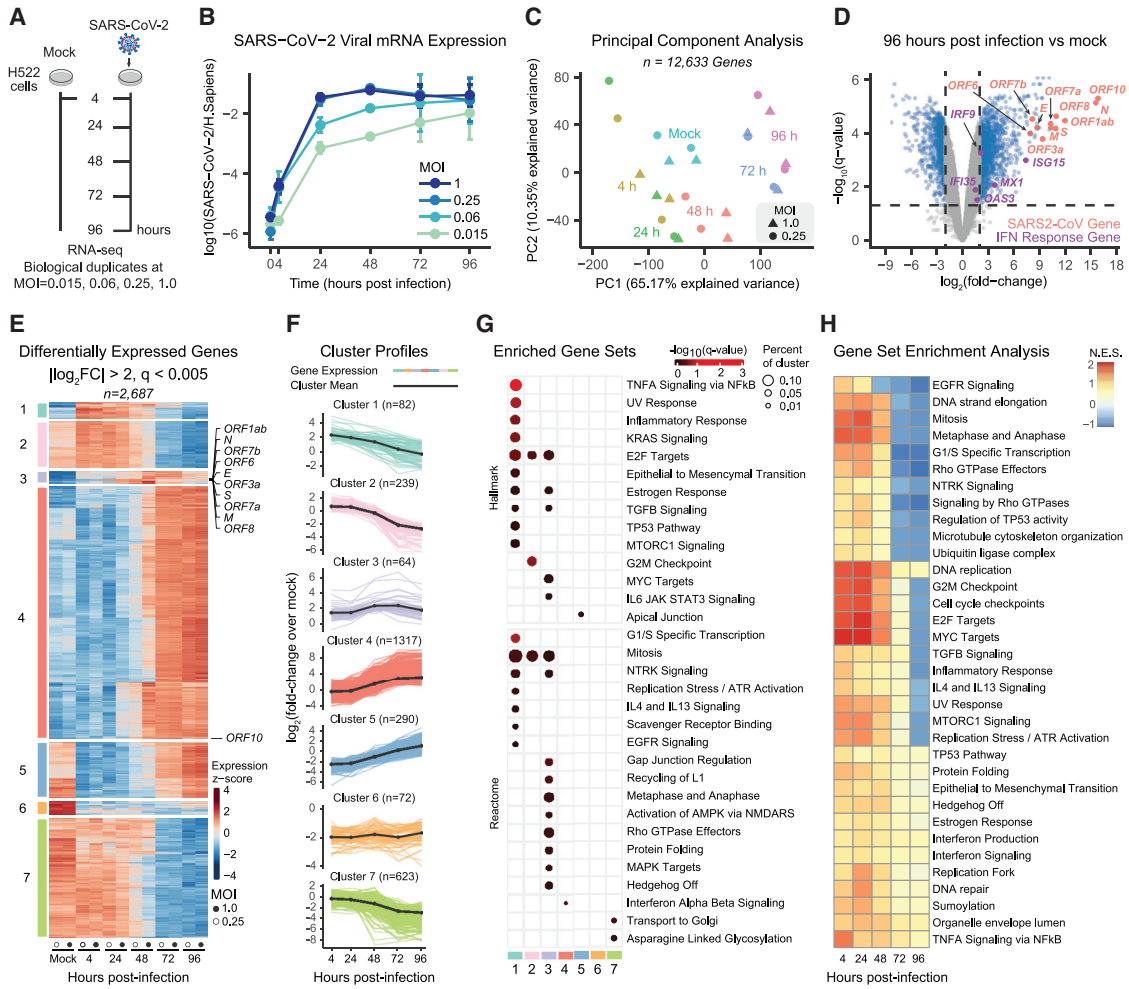

Figure 5. H522 transcriptomic response to SARS-CoV-2 infection

(A) Experimental design of transcriptomic experiments, performed in duplicate.

(B) Relative expression of SARS-CoV-2 RNA versus *H. sapiens* RNA from H522 (n = 2).

(C) Principal-component analysis (PCA) of highly expressed genes from MOIs of 0.25 and 1 across all time points.

(D) Volcano plot of gene expression changes comparing mock infection to 96 hpi of MOIs of 0.25 and 1. Selected changes in IFN response genes (purple) and SARS-CoV-2 genes (salmon) are highlighted. See also Table S3.

(E) Hierarchical clustering of differentially expressed genes (DEGs) after infection. Genes were filtered for an absolute $\log_2$ fold change >2 and adjusted p value <0.005 at any time point.

(F) Log_2 fold changes of DEGs as grouped by clustering. The colored lines represent quantification of an individual gene whereas a solid black line represents the cluster mean.

(G) Hypergeometric enrichment analysis of biological gene sets in the identified gene clusters (D and E). See also Table S4.

(H) Rank-based gene set enrichment analysis. Gene sets were queried when identified by hypergeometric analysis RNA-seq (F) or proteomics data (see Figure 6E). Display indicates p-adjusted < 0.05. N.E.S., normalized enrichment score.

separated well based on MOI and time after infection (Figure 5C). Analysis of differentially expressed genes (DEGs) at 96 hpi revealed MOI-dependent upregulation of IRF9, as well as numerous ISGs, including ISG15, MX1, IFI35, and OAS3 (Figure 5D; Table S3). Hierarchical consensus clustering of the 2,631 DEGs (|log fold change [FC]| > 2 and q < 0.005) generated seven temporally resolved clusters (Figures 5E and 5F). Overrepresentation analysis of each cluster revealed an initial sharp increase of cell cycle regulatory and inflammatory genes followed by decreasing levels as the infection proceeded (cluster 1) (Figures 5F and 5G; Table S4). Additionally, IFN-α/β signaling and downstream ISGs significantly increased as early as 48 hpi and continued to increase further by 96 hpi, consistent with high levels of SARS-CoV-2 infection (cluster 4; Figures 5E–5G; Table S4). Modulation of the cell cycle and sustained IFN signaling throughout infection were confirmed by gene set enrichment analysis (GSEA) of genes at each time point (Figure 5H; Table S4). Taken together, these findings highlight global changes in the H522 transcriptome in response to SARS-CoV-2 and marked induction of antiviral immune responses.

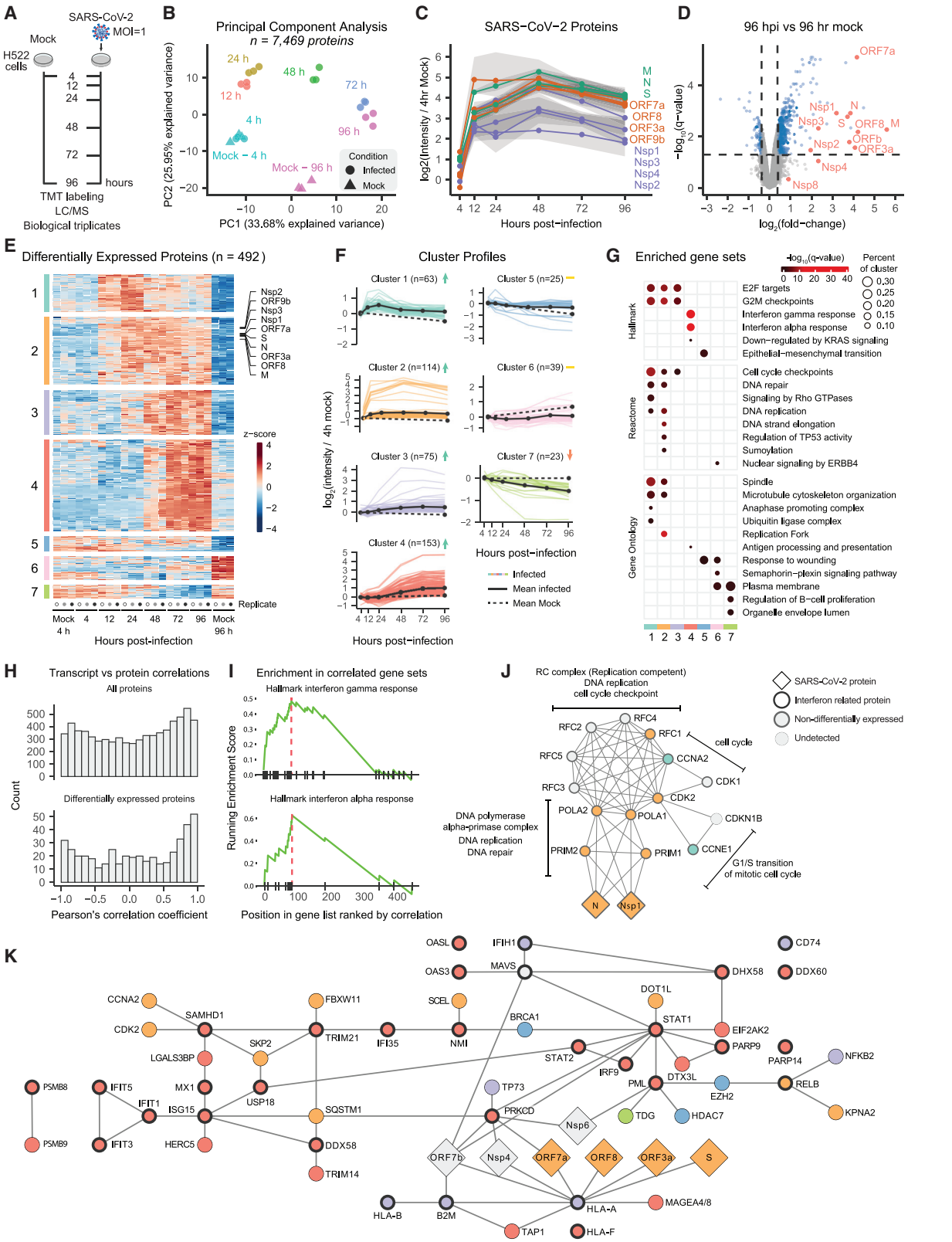

(legend on next page)

SARS-CoV-2-induced proteome changes in H522 cells reveal induction of type I IFN, cell cycle, and DNA replication pathways

To define the impact of SARS-CoV-2 infection on the H522 proteome, we conducted whole-cell quantitative proteomics experiments during the course of 4 days (Figure 6A). Biological triplicates for each time point were processed, and the abundance of 7,469 proteins was analyzed across samples. PCA highlights the high level of reproducibility and clustering of samples by infection and time post-infection (Figure 6B). Similar to viral RNAs, abundance of viral proteins increased substantially within the first 24 h of infection and plateaued thereafter (Figure 6C). At 96 hpi versus 96-h mock infection, 492 differentially expressed proteins were identified (Figure 6D). Unsupervised clustering defined seven unique clusters that characterize the temporal regulation of the H522 proteome (Figure 6E; Table S5). Overall, most of the differentially expressed proteins increased following SARS-CoV-2 infection, with proteins in cluster 4 displaying the greatest fold changes (Figure 6F; Table S5). Over-representation analysis revealed that cluster 4 proteins include those involved in the IFN-α and IFN-γ responses, which were the most significantly altered pathways (Figure 6G; Table S6). Of note, all viral proteins were present in cluster 2, and their accumulation preceded the induction of type I/III IFNs (Figure 6E). Cell cycle regulators were increased at early time points but declined thereafter, matching what was seen at the RNA level with a 12- to 24-h delay (cluster 1; Figures 6E–6G). In line with published studies (Bouhaddou et al., 2020; Ochsner et al., 2020), clusters 2 and 3 included proteins similarly involved in cell cycle regulation, DNA replication/repair, and microtubule organization but tended to remain upregulated during SARS-CoV-2 infection (Figures 6E–6G). Finally, clusters 6 and 7 included proteins that were downregulated and included plasma membrane proteins such as semaphorins (SEMA3A, SEMA3C, SEMA3D), APOE, ERBB4, LRP1, and SLIT2 with potential roles in viral entry pathways (Figures 6E–6G). We next looked for genes that correlated between our transcriptomic and proteomic datasets. Correlations were evenly distributed for the entire gene set; the subset of differentially expressed proteins shows increased correlation (Figure 6H). Among these genes, only the IFN-α and IFN-γ signaling pathways were identified by GSEA for enrichment in correlation, further supporting an IFN response in H522 cells to SARS-CoV-2 infection (Figure 6I).

To further illuminate pathways altered by SARS-CoV-2 infection, we mined the CORUM database for protein complexes consisting mostly of differentially expressed proteins (Figures 6J and S5). In total, 27 complexes were found and involved IFN signaling, cell cycle/DNA replication, DNA repair, epigenetic modification, and protein folding/ubiquitination (Figures 6J, 6K, and S5). More than half of the complexes had functions in cell cycle and DNA repair (n = 18). Of note, the viral proteins N and Nsp1 were previously reported to interact with components of the DNA polymerase alpha-primase complex, suggesting that the observed protein level changes may be a direct result of these interactions (Figure 6J). Additionally, we generated protein interaction networks based on BioGRID multi-validated datasets for the 492 differentially expressed proteins in H522 cells and the SARS-CoV-2 viral proteome (Figure 6K). A network emerged that contained 53 proteins involved in IFN signaling and downstream ISGs (Figure 6K). Seven viral proteins associate with various host proteins within this network, raising the possibility that SARS-CoV-2 may directly modulate the IFN response in H522 cells (Figure 6K). Taken together, these results show that SARS-CoV-2 infection of H522 cells leads to significant upregulation of several genes involved in innate immune pathways and cell cycle regulation at both the mRNA and protein levels.

MDA5 mediates the sensing of SARS-CoV-2 replication intermediates

To validate the IFN response, we measured the levels and activation of STAT1 and downstream ISGs in infected H522 cells. We found that SARS-CoV-2 replication induced STAT1 expression and its phosphorylation, as well as downstream ISGs, MX1, and IFIT1 by 48 hpi (Figure 7A). MX1 and IFIT1 were upregulated further as the infection progressed at 72 and 96 hpi (Figure 7A). Upregulation of the type I IFN response was delayed relative to the accumulation of viral N protein expression, which peaked by 24 hpi, possibly due to antagonism of host responses at early times in infection.

We next sought to define the mechanism by which H522 cells sense and respond to SARS-CoV-2 replication.

Figure 6. H522 infection with SARS-CoV-2 results in proteome changes within the type I IFN, cell cycle, and DNA replication pathways

(A) Experimental design of proteomic experiments. Peptides labeled with TMT10 reagents were analyzed by liquid chromatography-mass spectrometry.

(B) PCA of whole-cell proteomics of H522 cells infected with SARS-CoV-2 across a 4-day time course (n = 3).

(C) Quantification of total ion intensities for SARS-CoV-2 proteins over time and normalized to the 4-h mock control. The shaded gray regions represent SEM.

(D) Volcano plot of protein abundance at 96 hpi compared to the 96-h mock control. See also Table S5.

(E) Differentially expressed proteins from (D) were clustered based on the *Z* score.

(F) Quantification of total ion intensities normalized to the 4-h mock control for each protein across the seven identified clusters in (D). The colored lines represent quantification of an individual protein, whereas the solid black and dashed black lines represent the means of infected and mock samples, respectively.

(G) Hypergeometric enrichment analysis from three different databases for each individual cluster in (D) (Hallmark, Reactome, Gene Ontology [GO]). Color represents significance (q-value); size indicates the percentage of the cluster represented in the pathway. See also Table S6.

(H) Distribution of Pearson's correlation coefficient between a gene's transcript and protein $\log_2$ fold change over 4-h mock control for all proteins and differentially expressed proteins. Correlations used the matching time points of 4, 24, 48, 72, and 96 hpi.

(I) Rank-based gene set enrichment analysis. Differentially expressed proteins were ranked by their correlation to transcript levels.

(J) Protein complexes of differentially expressed H522 and SARS-CoV-2 proteins associated with DNA replication and cell cycle checkpoint. Complexes and functions were extracted from the CORUM database. The colors correspond to the whole-cell proteomic clusters identified in (D). See also Figure S5.

(K) Protein interaction network of differentially expressed H522 and SARS-CoV-2 proteins associated with the IFN response. Interactions were determined from the BioGRID multi-validated datasets. Interferon-related functions were extracted from GO terms in MSigDB. The colors correspond to the whole-cell proteomic clusters identified in (D). See also Figure S5.

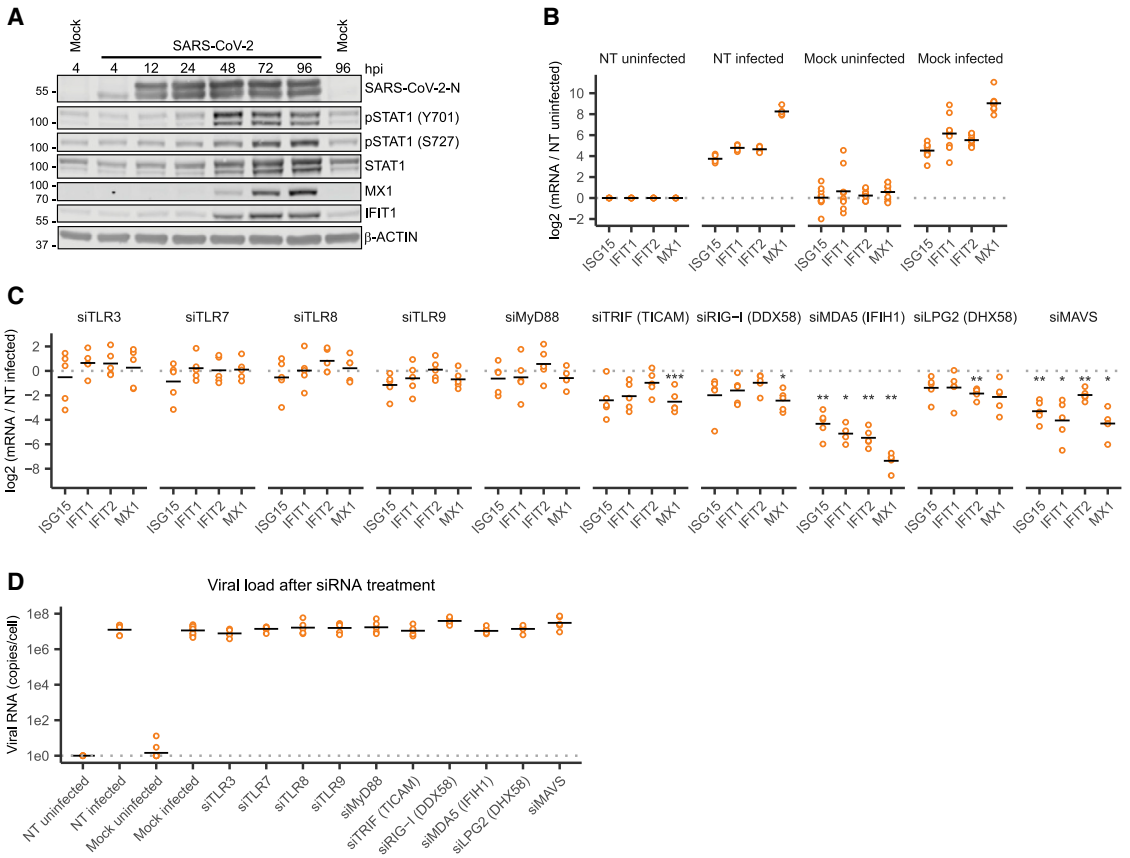

Figure 7. MDA5 mediates the IFN response to SARS-CoV-2 infection

(A) Immunoblot depicting the IFN response in H522 cells infected with SARS-CoV-2 over time (representative of n = 2).

(B) H522 cells were either mock transfected or transfected with a NT siRNA 24 h prior to infection. qRT-PCR analysis of ISG expression in H522 cells infected with SARS-CoV-2 (MOI of 1) at 96 hpi is shown.

(C) H522 cells were transfected with a NT siRNA or a panel of siRNAs targeting genes involved in RNA sensing 24 h prior to infection. ISG mRNA levels were detected by qRT-PCR in H522 cells infected with SARS-CoV-2 at 96 hpi. *p < 0.05, **p < 0.01, ***p < 0.001 compared to NT using two-way ANOVA and Dunnett's correction for multiple comparisons. See also Figure S6.

(D) qRT-PCR for cell-associated SARS-CoV-2 RNA in H522 cells (96 hpi) following siRNA transfection as in (C).

Components of TLR and RLR-dependent sensing pathways were depleted by siRNA transfection, and upregulation of ISGs were assessed following SARS-CoV-2 infection. Most targets remained efficiently silenced up to 120 h after siRNA transfection (Figure S6). The low silencing efficiency of TLR3, TLR7, TLR8, and TLR9 is most likely due to their low to undetectable basal expression levels (Figure S6). Consistent with RNA-seq and proteomics findings, ISG15, IFIT1, IFIT2, and MX1 were upregulated upon infection in mock- and non-targeting (NT) siRNA-transfected H522 cells (Figure 7B). Depletion of MDA5, and to a lesser extent the downstream adaptor MAVS, significantly reduced ISG induction in response to SARS-CoV-2 infection (Figure 7C). Knockdown of other host defense targets had little or no impact on ISG upregulation (Figure 7C). Despite the decreased IFN response in MDA5- and MAVS-depleted H522 cells, SARS-CoV-2 viral RNA levels remained at similar levels compared to controls (Figure 7D). Taken together, these results together suggest that viral RNAs are sensed by components of the RLR pathway in H522s, resulting in activation of the type I IFN response.

DISCUSSION

Our screen of human lung and head/neck cancer cell lines expressing varying levels of ACE2 and TMPRSS2 identified the H522 human lung adenocarcinoma cell line as being naturally permissive to SARS-CoV-2 infection despite no evidence of detectable ACE2 and TMPRSS2 expression. Using orthogonal assays, we confirmed the ACE2 independence of H522 infection, which suggests the utilization of an alternative receptor in a cell line of lung origin. As ACE2 expression is comparably low in the human respiratory system (Aguiar et al., 2020; Hikmet et al., 2020), other co-receptors and/or attachment factors have been suspected to facilitate viral entry. Indeed, recent findings establish NRP1, AXL, and heparan sulfate as mediators of ACE2-dependent SARS-CoV-2 entry (Cantuti-Castelvetri et al., 2020; Clausen et al., 2020; Daly et al., 2020; Wang et al.,

2021). We found that SARS-CoV-2 infection of H522 cells is independent of NRP1 and AXL but dependent on heparan sulfate. Coronaviruses can utilize a diverse array of glycoconjugates as attachment factors, such as 9-*O*-Ac-sialosides (Huang et al., 2015; Hulswit et al., 2019; Tortorici et al., 2019) as well as other sialoglycans distinct from 9-*O*-Ac-sialosides (Li et al., 2017; Liu et al., 2015; Park et al., 2019; Schultze et al., 1996; Vlasak et al., 1988; Wickramasinghe et al., 2011). Whether sialic acids can also serve as entry receptors or whether a host protein modified by heparan sulfates mediates SARS-CoV-2 entry in H522 cells remains to be determined.

Despite the possible utilization of an alternative receptor, SARS-CoV-2 entry into H522 cells requires S, and the E484D S substitution appears to be specifically required for viral entry into H522 cells. However, the low level of infectivity with the lentiviral pseudoparticles and the inability of the VSV-GFP-SARS-CoV-2 E484D to spread suggests that other factors, viral or cellular, may be required for efficient virus replication in H522 cells. VSV is highly sensitive to type I IFNs, and numerous ISGs have been documented to block VSV replication (Espert et al., 2003; Fensterl et al., 2012; Liu et al., 2012; Müller et al., 1994; Pavlovic et al., 1990; Rihn et al., 2019; Rubinstein et al., 1981; Zürcher et al., 1992). The ability of VSV-GFP-SARS-CoV-2-$S_{\Delta 21}$ to infect H522 cells upon ACE2 expression argues against the possibility of intrinsic and IFN-induced innate immune factors limiting VSV infection in H522 cells. In a complementary experiment, inhibition of type I IFN signaling by ruxolitinib (a JAK1/2 inhibitor) did not facilitate the spread of VSV-GFP-SARS-CoV-2-$S_{\Delta 21}$ or the E484D mutant (data not shown). Whether the viral coat E and M proteins functionally impact infection of H522 remains to be tested (Masters, 2006; Schoeman and Fielding, 2019), as it is plausible that the steric hindrance caused by blockage of S by antibodies may have interfered with E/M-mediated entry.

Since its emergence, numerous substitutions within S have been isolated from humans, some with clear associations with enhanced transmissibility and increased pathogenicity (Peacock et al., 2021). Substitutions within the E484 position, including E484D/K/Q/A/G, have been found in naturally circulating SARS-CoV-2 isolates as well as in clinical settings in response to mAb treatment. Furthermore, substitutions at position E484 also were found to confer resistance to neutralization by convalescent human sera as well as neutralizing antibodies in cell culture (Chen et al., 2021; Liu et al., 2021; Weisblum et al., 2020). Our studies suggest that the E484D substitution may enable SARS-CoV-2 the ability to use an alternative receptor, either heparan sulfate alone or a modified host protein, without impacting ACE2-dependent entry. Thus, our findings have key implications for SARS-CoV-2 pathogenesis and tropism given the key role of sulfated glycosaminoglycans in lung development and function (Haeger et al., 2016).

Another important observation in our study is the inability of numerous lung and head/neck cancer cell lines to support SARS-CoV-2 replication, despite expressing ACE2/TMPRSS2. The one exception was HCC827 cells, which express ACE2/TMPRSS2 but were less permissive to infection than H522 and Vero E6 cells. One possible explanation for the general lack of permissiveness of these cell lines to SARS-CoV-2 include potential alternative glycosylation or other post-translational modifications of ACE2 (Figure 1C). Alternatively, the presence or induction of antiviral mechanisms such as type I/III IFNs and ISGs may inhibit SARS-CoV-2 replication in these cells. These results collectively suggest that expression of ACE2/TMPRSS2 at endogenous levels does not directly predict permissiveness to SARS-CoV-2 infection.

We posit that the lower susceptibility of H522 cells as compared to Vero E6 cells may be explained by the ability to mount a substantial type I IFN response upon infection (Figures 5, 6, and 7). This hypothesis agrees with previous studies demonstrating the potent inhibition of SARS-CoV-2 replication by type I IFN treatment *in vitro* (Lokugamage et al., 2020; Xie et al., 2020). Furthermore, similar to Calu-3 cells (Yin et al., 2021), we found clear involvement of MDA5 and MAVS in the induction of the IFN response in H522 cells. Despite the marked activation of the type I IFN responses, virus spread in H522 cells suggests the effective antagonism of these antiviral responses, possibly through the actions of numerous viral proteins (Park and Iwasaki, 2020).

Several CoV proteins have well-described functions in modulating host gene expression post-transcriptionally (Huang et al., 2011; Kamitani et al., 2009; Kopecky-Bromberg et al., 2006; Lokugamage et al., 2012; Nakagawa et al., 2016; Narayanan et al., 2008; Xiao et al., 2008; Zhou et al., 2008). For example, SARS-CoV-2 Nsp1 is thought to block host mRNA translation through its direct binding to host ribosomes (Schubert et al., 2020; Yuan et al., 2020), which may explain the discordance of host responses between existing RNA-seq and proteomics studies in SARS-CoV-2-infected cells (Blanco-Melo et al., 2020; Bojkova et al., 2020; Bouhaddou et al., 2020; Chu et al., 2020a; Mick et al., 2020; Stukalov et al., 2020). Similarly, we observed a range of anti-correlated and correlated regulated genes from our transcriptomic and proteomic datasets (Figure 6H), further supporting a role for SARS-CoV-2 in modulating the host cell translational response, possibly through the action of Nsp1 or other viral proteins.

Our data implicate CME in SARS-CoV-2 infection of H522 cells. Specific inhibition of a kinase directly involved in CME, AAK1, reduced SARS-CoV-2 infection in H522 cells and patient-derived HBECs (Figures 4 and S4). Although inhibition of AAK1 and CME have been suggested for therapeutic treatment of COVID-19, their efficacy has not been established. AAK1 inhibition preferentially blocked SARS-CoV-2 infection in H522 cells as compared to Vero E6 or Calu-3 cells (Figure S4), suggesting that the ACE2-independent, heparan sulfate-dependent entry mechanism in H522 cells relies on CME.

Taken together, H522 cells provide an alternative *in vitro* model to study SARS-CoV-2 infection and host innate immune responses. The independence of virus replication from ACE2/TMPRSS2 in these cells indicates the utilization of a heparan sulfate-linked alternative receptor complex and entry pathway. The striking requirement of the S E484D variant for infection of H522 cells establishes possible physiological relevance to these findings, which may reveal new facets of disease pathogenesis *in vivo*, particularly as it relates to variants. Characterization of these mechanisms may provide unique targets for therapeutic development and vaccine design. The inevitable emergence of

novel coronaviruses utilizing variable entry pathways highlights the importance of the H522 cell line model.

Limitations of the study

Many of the experiments in this study used cell-associated viral RNA levels as a proxy for viral entry. Advanced microscopy approaches would directly assess viral entry in H522 cells. Determining the *in vivo* relevance of the alternative entry mechanism identified in our study will depend on identification of the receptor utilized in H522 cells. Profiling the expression pattern of this receptor *in vivo* and evaluating its impact in animal models of disease will be crucial to establish its relevance to SARS-CoV-2 pathogenesis in humans. This study does not establish why the E484D variant enables ACE2-independent infection. Once the novel receptor mechanism is known, structural and biochemical studies of E484D S will be important.

STAR★METHODS

Detailed methods are provided in the online version of this paper and include the following:

- KEY RESOURCES TABLE
- RESOURCE AVAILABILITY
  - Lead contact
  - Materials availability
  - Data and code availability
- EXPERIMENTAL MODEL AND SUBJECT DETAILS
  - Viral strains
  - Cell culture
- METHOD DETAILS
  - Cloning
  - Lentivirus production and transduction
  - SARS-CoV-2 infections, plaque assays, and FACS
  - RNA extraction, qRT-PCR, and RNA-seq
  - Immunofluorescence, RNA-ISH, and transmission electron microscopy
  - Live cell imaging and quantification
  - Immunoblotting
  - CRISPR KO
  - siRNA transfections
  - Pharmacological, neutralizing antibody, and sera effects on SARS-CoV-2 infections
  - Monoclonal antibody generation
  - NTD-binding ELISA
  - Removal of heparan sulfates from cell surface
  - Whole-cell proteomics sample preparation
  - Mass spectrometry data acquisition
  - Whole-cell proteomics raw data processing
- QUANTIFICATION AND STATISTICAL ANALYSIS
  - RNA-seq data
  - Whole-cell proteomics data
  - Cluster analysis
  - Gene set enrichment analysis

SUPPLEMENTAL INFORMATION

Supplemental information can be found online at https://doi.org/10.1016/j.celrep.2021.109364.

ACKNOWLEDGMENTS

This work was supported by Washington University funds to S.B.K., a V Foundation grant (T2014-009) to M.B.M. and D.N.H., a T32 training grant (T32CA009547-34) to K.M.L., a T32 training grant (5T32HL007106-39) to E.M.C., the Dorothy R. and Hubert C. Moog Professor of Medicine to S.L.B., a K08HL150223 grant to A.H., NIH AI059371 to S.P.J.W., NIH R01 AI157155 to M.S.D., NIH 75N93019C00074, NIH R01 AI157155, and the Defense Advanced Research Projects Agency (HR001117S0019) grants to J.E.C. This study utilized samples obtained from the Washington University School of Medicine's COVID-19 biorepository supported by NIH/National Center for Advancing Translational Sciences grant UL1 TR002345. We thank Drs. Ali Ellebedy, Rachel Presti, Jane O'Halloran, Daved Fremont, and Paul D. Bieniasz for key reagents utilized in the study, including neutralizing antibodies, sera from vaccine recipients, convalescent sera, Fc-ACE2, and plasmids. We additionally thank other members of the Whelan and Diamond laboratories for reagents.

AUTHOR CONTRIBUTIONS

M.P.-C., K.M.L., M.B.M., and S.B.K. conceptualized the study; M.P.-C., K.M.L., M.B.M., and S.B.K. designed the methodology. M.P.-C., K.M.L., J.L.E., D.P.B., M.J.A., D.Q.L., K.D., K.T., J.E.E., C.S.M., H.R.V., E.M.C., E.W.C., and S.B.K performed the experiments. T.P.S., R.J., H.J., and D.G. performed all statistical and bioinformatics analyses with help from N.L. and K.T. P.W.R., Z.L., A.L.B., L.A.V., M.S.D., P.G., and J.E.C. generated and provided key reagents. A.H. and S.L.B. generated and cultured primary basal epithelial cells. K.M.L., M.B.M., and S.B.K. wrote the manuscript with input from all of the authors.

DECLARATION OF INTERESTS

S.P.J.W., P.W.R., and Washington University have filed a patent application for uses of VSV-SARS-CoV-2. S.P.J.W. has received unrelated funding support in sponsored research agreements with Vir Biotechnology, Abbvie, and SAB therapeutics. M.S.D. is a consultant for Inbios, Vir Biotechnology, Fortress Biotech, and Carnival Corporation, and is on the Scientific Advisory Boards of Moderna and Immunome. The Diamond laboratory has received funding support in sponsored research agreements from Moderna, Vir Biotechnology, Kaleido, and Emergent BioSolutions. J.E.C. has served as a consultant for Luna Biologics, is a member of the Scientific Advisory Boards of Meissa Vaccines, and is Founder of IDBiologics. The Crowe laboratory has received sponsored research agreements from Takeda, AstraZeneca, and IDBiologics. Vanderbilt University has applied for patents related to antibodies described in this paper. The remaining authors declare no competing interests.

Received: February 4, 2021
Revised: May 25, 2021
Accepted: June 17, 2021
Published: July 13, 2021

REFERENCES

Agajanian, M.J., Walker, M.P., Axtman, A.D., Ruela-de-Sousa, R.R., Serafin, D.S., Rabinowitz, A.D., Graham, D.M., Ryan, M.B., Tamir, T., Nakamichi, Y., et al. (2019). WNT activates the AAK1 kinase to promote clathrin-mediated endocytosis of LRP6 and establish a negative feedback loop. Cell Rep. *26*, 79–93.e8.

Aguiar, J.A., Tremblay, B.J., Mansfield, M.J., Woody, O., Lobb, B., Banerjee, A., Chandiramohan, A., Tiessen, N., Cao, Q., Dvorkin-Gheva, A., et al. (2020). Gene expression and *in situ* protein profiling of candidate SARS-CoV-2 receptors in human airway epithelial cells and lung tissue. Eur. Respir. J. *56*, 2001123.

Alsoussi, W.B., Turner, J.S., Case, J.B., Zhao, H., Schmitz, A.J., Zhou, J.Q., Chen, R.E., Lei, T., Rizk, A.A., McIntire, K.M., et al. (2020). A potently

neutralizing antibody protects mice against SARS-CoV-2 infection. J. Immunol. *205*, 915–922.

Amraie, R., Napoleon, M.A., Yin, W., Berrigan, J., Suder, E., Zhao, G., Olejnik, J., Gummuluru, S., Muhlberger, E., Chitalia, V., et al. (2020). CD209L/L-SIGN and CD209/DC-SIGN act as receptors for SARS-CoV-2 and are differentially expressed in lung and kidney epithelial and endothelial cells. bioRxiv. https://doi.org/10.1101/2020.06.22.165803.

Blanco-Melo, D., Nilsson-Payant, B.E., Liu, W.C., Uhl, S., Hoagland, D., Møller, R., Jordan, T.X., Oishi, K., Panis, M., Sachs, D., et al. (2020). Imbalanced host response to SARS-CoV-2 drives development of COVID-19. Cell *181*, 1036–1045.e9.

Bojkova, D., Klann, K., Koch, B., Widera, M., Krause, D., Ciesek, S., Cinatl, J., and Münch, C. (2020). Proteomics of SARS-CoV-2-infected host cells reveals therapy targets. Nature *583*, 469–472.

Bouhaddou, M., Memon, D., Meyer, B., White, K.M., Rezelj, V.V., Correa Marrero, M., Polacco, B.J., Melnyk, J.E., Ulferts, S., Kaake, R.M., et al. (2020). The global phosphorylation landscape of SARS-CoV-2 infection. Cell *182*, 685–712.e19.

Cagno, V. (2020). SARS-CoV-2 cellular tropism. Lancet Microbe *1*, e2–e3.

Cantuti-Castelvetri, L., Ojha, R., Pedro, L.D., Djannatian, M., Franz, J., Kuivanen, S., van der Meer, F., Kallio, K., Kaya, T., Anastasina, M., et al. (2020). Neuropilin-1 facilitates SARS-CoV-2 cell entry and infectivity. Science *370*, 856–860.

Case, J.B., Rothlauf, P.W., Chen, R.E., Liu, Z., Zhao, H., Kim, A.S., Bloyet, L.M., Zeng, Q., Tahan, S., Droit, L., et al. (2020). Neutralizing antibody and soluble ACE2 inhibition of a replication-competent VSV-SARS-CoV-2 and a clinical isolate of SARS-CoV-2. Cell Host Microbe *28*, 475–485.e5.

Chen, G., Wu, D., Guo, W., Cao, Y., Huang, D., Wang, H., Wang, T., Zhang, X., Chen, H., Yu, H., et al. (2020). Clinical and immunological features of severe and moderate coronavirus disease 2019. J. Clin. Invest. *130*, 2620–2629.

Chen, R.E., Zhang, X., Case, J.B., Winkler, E.S., Liu, Y., VanBlargan, L.A., Liu, J., Errico, J.M., Xie, X., Suryadevara, N., et al. (2021). Resistance of SARS-CoV-2 variants to neutralization by monoclonal and serum-derived polyclonal antibodies. Nat. Med. *27*, 717–726.

Chu, H., Chan, J.F., Wang, Y., Yuen, T.T., Chai, Y., Hou, Y., Shuai, H., Yang, D., Hu, B., Huang, X., et al. (2020a). Comparative replication and immune activation profiles of SARS-CoV-2 and SARS-CoV in human lungs: An ex vivo study with implications for the pathogenesis of COVID-19. Clin. Infect. Dis. *71*, 1400–1409.

Chu, H., Chan, J.F.-W., Yuen, T.T.-T., Shuai, H., Yuan, S., Wang, Y., Hu, B., Yip, C.C.-Y., Tsang, J.O.-L., Huang, X., et al. (2020b). Comparative tropism, replication kinetics, and cell damage profiling of SARS-CoV-2 and SARS-CoV with implications for clinical manifestations, transmissibility, and laboratory studies of COVID-19: An observational study. Lancet Microbe *1*, e14–e23.

Clausen, T.M., Sandoval, D.R., Spliid, C.B., Pihl, J., Perrett, H.R., Painter, C.D., Narayanan, A., Majowicz, S.A., Kwong, E.M., McVicar, R.N., et al. (2020). SARS-CoV-2 infection depends on cellular heparan sulfate and ACE2. Cell *183*, 1043–1057.e15.

Conner, S.D., and Schmid, S.L. (2002). Identification of an adaptor-associated kinase, AAK1, as a regulator of clathrin-mediated endocytosis. J. Cell Biol. *156*, 921–929.

Conner, S.D., and Schmid, S.L. (2003). Differential requirements for AP-2 in clathrin-mediated endocytosis. J. Cell Biol. *162*, 773–779.

Daly, J.L., Simonetti, B., Klein, K., Chen, K.E., Williamson, M.K., Antón-Plágaro, C., Shoemark, D.K., Simón-Gracia, L., Bauer, M., Hollandi, R., et al. (2020). Neuropilin-1 is a host factor for SARS-CoV-2 infection. Science *370*, 861–865.

Desmyter, J., Melnick, J.L., and Rawls, W.E. (1968). Defectiveness of interferon production and of rubella virus interference in a line of African green monkey kidney cells (Vero). J. Virol. *2*, 955–961.

Diaz, M.O., Ziemin, S., Le Beau, M.M., Pitha, P., Smith, S.D., Chilcote, R.R., and Rowley, J.D. (1988). Homozygous deletion of the alpha- and beta 1-interferon genes in human leukemia and derived cell lines. Proc. Natl. Acad. Sci. USA *85*, 5259–5263.

Espert, L., Degols, G., Gongora, C., Blondel, D., Williams, B.R., Silverman, R.H., and Mechti, N. (2003). ISG20, a new interferon-induced RNase specific for single-stranded RNA, defines an alternative antiviral pathway against RNA genomic viruses. J. Biol. Chem. *278*, 16151–16158.

Fensterl, V., Wetzel, J.L., Ramachandran, S., Ogino, T., Stohlman, S.A., Bergmann, C.C., Diamond, M.S., Virgin, H.W., and Sen, G.C. (2012). Interferon-induced *Ifit2/ISG54* protects mice from lethal VSV neuropathogenesis. PLoS Pathog. *8*, e1002712.

Gao, C., Zeng, J., Jia, N., Stavenhagen, K., Matsumoto, Y., Zhang, H., Li, J., Hume, A.J., Muhlberger, E., van Die, I., et al. (2020). SARS-CoV-2 spike protein interacts with multiple innate immune receptors. bioRxiv. https://doi.org/10.1101/2020.07.29.227462.

Giurgiu, M., Reinhard, J., Brauner, B., Dunger-Kaltenbach, I., Fobo, G., Frishman, G., Montrone, C., and Ruepp, A. (2019). CORUM: The comprehensive resource of mammalian protein complexes—2019. Nucleic Acids Res. *47* (*D1*), D559–D563.

Haeger, S.M., Yang, Y., and Schmidt, E.P. (2016). Heparan sulfate in the developing, healthy, and injured lung. Am. J. Respir. Cell Mol. Biol. *55*, 5–11.

Hamming, I., Timens, W., Bulthuis, M.L., Lely, A.T., Navis, G., and van Goor, H. (2004). Tissue distribution of ACE2 protein, the functional receptor for SARS coronavirus. A first step in understanding SARS pathogenesis. J. Pathol. *203*, 631–637.

Hikmet, F., Méar, L., Edvinsson, Å., Micke, P., Uhlén, M., and Lindskog, C. (2020). The protein expression profile of ACE2 in human tissues. Mol. Syst. Biol. *16*, e9610.

Hoffmann, M., Kleine-Weber, H., Schroeder, S., Krüger, N., Herrler, T., Erichsen, S., Schiergens, T.S., Herrler, G., Wu, N.H., Nitsche, A., et al. (2020). SARS-CoV-2 cell entry depends on ACE2 and TMPRSS2 and is blocked by a clinically proven protease inhibitor. Cell *181*, 271–280.e8.

Horani, A., Druley, T.E., Zariwala, M.A., Patel, A.C., Levinson, B.T., Van Arendonk, L.G., Thornton, K.C., Giacalone, J.C., Albee, A.J., Wilson, K.S., et al. (2012). Whole-exome capture and sequencing identifies *HEATR2* mutation as a cause of primary ciliary dyskinesia. Am. J. Hum. Genet. *91*, 685–693.

Horani, A., Nath, A., Wasserman, M.G., Huang, T., and Brody, S.L. (2013). Rho-associated protein kinase inhibition enhances airway epithelial basal-cell proliferation and lentivirus transduction. Am. J. Respir. Cell Mol. Biol. *49*, 341–347.

Horani, A., Ustione, A., Huang, T., Firth, A.L., Pan, J., Gunsten, S.P., Haspel, J.A., Piston, D.W., and Brody, S.L. (2018). Establishment of the early cilia preassembly protein complex during motile ciliogenesis. Proc. Natl. Acad. Sci. USA *115*, E1221–E1228.

Hou, Y.J., Okuda, K., Edwards, C.E., Martinez, D.R., Asakura, T., Dinnon, K.H., 3rd, Kato, T., Lee, R.E., Yount, B.L., Mascenik, T.M., et al. (2020). SARS-CoV-2 reverse genetics reveals a variable infection gradient in the respiratory tract. Cell *182*, 429–446.e14.

Huang, C., Lokugamage, K.G., Rozovics, J.M., Narayanan, K., Semler, B.L., and Makino, S. (2011). SARS coronavirus nsp1 protein induces template-dependent endonucleolytic cleavage of mRNAs: Viral mRNAs are resistant to nsp1-induced RNA cleavage. PLoS Pathog. *7*, e1002433.

Huang, X., Dong, W., Milewska, A., Golda, A., Qi, Y., Zhu, Q.K., Marasco, W.A., Baric, R.S., Sims, A.C., Pyrc, K., et al. (2015). Human coronavirus hku1 spike protein uses *O*-acetylated sialic acid as an attachment receptor determinant and employs hemagglutinin-esterase protein as a receptor-destroying enzyme. J. Virol. *89*, 7202–7213.

Huang, C., Wang, Y., Li, X., Ren, L., Zhao, J., Hu, Y., Zhang, L., Fan, G., Xu, J., Gu, X., et al. (2020). Clinical features of patients infected with 2019 novel coronavirus in Wuhan, China. Lancet *395*, 497–506.

Hulswit, R.J.G., Lang, Y., Bakkers, M.J.G., Li, W., Li, Z., Schouten, A., Ophorst, B., van Kuppeveld, F.J.M., Boons, G.J., Bosch, B.J., et al. (2019). Human coronaviruses OC43 and HKU1 bind to 9-*O*-acetylated sialic acids via a conserved receptor-binding site in spike protein domain A. Proc. Natl. Acad. Sci. USA *116*, 2681–2690.

Jassal, B., Matthews, L., Viteri, G., Gong, C., Lorente, P., Fabregat, A., Sidiropoulos, K., Cook, J., Gillespie, M., Haw, R., et al. (2020). The reactome pathway knowledgebase. Nucleic Acids Res. *48* (*D1*), D498–D503.

Kamitani, W., Huang, C., Narayanan, K., Lokugamage, K.G., and Makino, S. (2009). A two-pronged strategy to suppress host protein synthesis by SARS coronavirus Nsp1 protein. Nat. Struct. Mol. Biol. *16*, 1134–1140.

Kang, Y.L., Chou, Y.Y., Rothlauf, P.W., Liu, Z., Soh, T.K., Cureton, D., Case, J.B., Chen, R.E., Diamond, M.S., Whelan, S.P.J., and Kirchhausen, T. (2020). Inhibition of PIKfyve kinase prevents infection by Zaire ebolavirus and SARS-CoV-2. Proc. Natl. Acad. Sci. USA *117*, 20803–20813.

Kim, J.M., Chung, Y.S., Jo, H.J., Lee, N.J., Kim, M.S., Woo, S.H., Park, S., Kim, J.W., Kim, H.M., and Han, M.G. (2020). Identification of coronavirus isolated from a patient in Korea with COVID-19. Osong Public Health Res. Perspect. *11*, 3–7.

Kopecky-Bromberg, S.A., Martinez-Sobrido, L., and Palese, P. (2006). 7a protein of severe acute respiratory syndrome coronavirus inhibits cellular protein synthesis and activates p38 mitogen-activated protein kinase. J. Virol. *80*, 785–793.

Lazear, H.M., Schoggins, J.W., and Diamond, M.S. (2019). Shared and distinct functions of type I and type III interferons. Immunity *50*, 907–923.

Letko, M., Marzi, A., and Munster, V. (2020). Functional assessment of cell entry and receptor usage for SARS-CoV-2 and other lineage B betacoronaviruses. Nat. Microbiol. *5*, 562–569.

Li, W., Hulswit, R.J.G., Widjaja, I., Raj, V.S., McBride, R., Peng, W., Widagdo, W., Tortorici, M.A., van Dieren, B., Lang, Y., et al. (2017). Identification of sialic acid-binding function for the Middle East respiratory syndrome coronavirus spike glycoprotein. Proc. Natl. Acad. Sci. USA *114*, E8508–E8517.

Liberzon, A., Subramanian, A., Pinchback, R., Thorvaldsdóttir, H., Tamayo, P., and Mesirov, J.P. (2011). Molecular Signatures Database (MSigDB) 3.0. Bioinformatics *27*, 1739–1740.

Liberzon, A., Birger, C., Thorvaldsdóttir, H., Ghandi, M., Mesirov, J.P., and Tamayo, P. (2015). The Molecular Signatures Database (MSigDB) hallmark gene set collection. Cell Syst. *1*, 417–425.

Liu, S.Y., Sanchez, D.J., Aliyari, R., Lu, S., and Cheng, G. (2012). Systematic identification of type I and type II interferon-induced antiviral factors. Proc. Natl. Acad. Sci. USA *109*, 4239–4244.

Liu, C., Tang, J., Ma, Y., Liang, X., Yang, Y., Peng, G., Qi, Q., Jiang, S., Li, J., Du, L., and Li, F. (2015). Receptor usage and cell entry of porcine epidemic diarrhea coronavirus. J. Virol. *89*, 6121–6125.

Liu, Z., VanBlargan, L.A., Bloyet, L.M., Rothlauf, P.W., Chen, R.E., Stumpf, S., Zhao, H., Errico, J.M., Theel, E.S., Liebeskind, M.J., et al. (2021). Identification of SARS-CoV-2 spike mutations that attenuate monoclonal and serum antibody neutralization. Cell Host Microbe *29*, 477–488.e4.

Lokugamage, K.G., Narayanan, K., Huang, C., and Makino, S. (2012). Severe acute respiratory syndrome coronavirus protein nsp1 is a novel eukaryotic translation inhibitor that represses multiple steps of translation initiation. J. Virol. *86*, 13598–13608.

Lokugamage, K.G., Hage, A., de Vries, M., Valero-Jimenez, A.M., Schindewolf, C., Dittmann, M., Rajsbaum, R., and Menachery, V.D. (2020). Type I interferon susceptibility distinguishes SARS-CoV-2 from SARS-CoV. J. Virol. *94*, e01410-20.

Long, J.S., Mistry, B., Haslam, S.M., and Barclay, W.S. (2019). Host and viral determinants of influenza A virus species specificity. Nat. Rev. Microbiol. *17*, 67–81.

Malim, M.H., and Bieniasz, P.D. (2012). HIV restriction factors and mechanisms of evasion. Cold Spring Harb. Perspect. Med. *2*, a006940.

Masters, P.S. (2006). The molecular biology of coronaviruses. Adv. Virus Res. *66*, 193–292.

Mertins, P., Tang, L.C., Krug, K., Clark, D.J., Gritsenko, M.A., Chen, L., Clauser, K.R., Clauss, T.R., Shah, P., Gillette, M.A., et al. (2018). Reproducible workflow for multiplexed deep-scale proteome and phosphoproteome analysis of tumor tissues by liquid chromatography-mass spectrometry. Nat. Protoc. *13*, 1632–1661.

Mick, E., Kamm, J., Pisco, A.O., Ratnasiri, K., Babik, J.M., Castañeda, G., DeRisi, J.L., Detweiler, A.M., Hao, S.L., Kangelaris, K.N., et al. (2020). Upper airway gene expression reveals suppressed immune responses to SARS-CoV-2 compared with other respiratory viruses. Nat. Commun. *11*, 5854.

Müller, U., Steinhoff, U., Reis, L.F., Hemmi, S., Pavlovic, J., Zinkernagel, R.M., and Aguet, M. (1994). Functional role of type I and type II interferons in antiviral defense. Science *264*, 1918–1921.

Nakagawa, K., Lokugamage, K.G., and Makino, S. (2016). Viral and cellular mRNA translation in coronavirus-infected cells. Adv. Virus Res. *96*, 165–192.

Narayanan, K., Huang, C., Lokugamage, K., Kamitani, W., Ikegami, T., Tseng, C.T., and Makino, S. (2008). Severe acute respiratory syndrome coronavirus nsp1 suppresses host gene expression, including that of type I interferon, in infected cells. J. Virol. *82*, 4471–4479.

Ochsner, S.A., Pillich, R.T., and McKenna, N.J. (2020). Consensus transcriptional regulatory networks of coronavirus-infected human cells. Sci. Data *7*, 314.

Osada, N., Kohara, A., Yamaji, T., Hirayama, N., Kasai, F., Sekizuka, T., Kuroda, M., and Hanada, K. (2014). The genome landscape of the African green monkey kidney-derived Vero cell line. DNA Res. *21*, 673–683.

Ou, X., Liu, Y., Lei, X., Li, P., Mi, D., Ren, L., Guo, L., Guo, R., Chen, T., Hu, J., et al. (2020). Characterization of spike glycoprotein of SARS-CoV-2 on virus entry and its immune cross-reactivity with SARS-CoV. Nat. Commun. *11*, 1620.

Oughtred, R., Rust, J., Chang, C., Breitkreutz, B.J., Stark, C., Willems, A., Boucher, L., Leung, G., Kolas, N., Zhang, F., et al. (2021). The BioGRID database: A comprehensive biomedical resource of curated protein, genetic, and chemical interactions. Protein Sci. *30*, 187–200.

Park, A., and Iwasaki, A. (2020). Type I and type III interferons—Induction, signaling, evasion, and application to combat COVID-19. Cell Host Microbe *27*, 870–878.

Park, Y.J., Walls, A.C., Wang, Z., Sauer, M.M., Li, W., Tortorici, M.A., Bosch, B.J., DiMaio, F., and Veesler, D. (2019). Structures of MERS-CoV spike glycoprotein in complex with sialoside attachment receptors. Nat. Struct. Mol. Biol. *26*, 1151–1157.

Patro, R., Duggal, G., Love, M.I., Irizarry, R.A., and Kingsford, C. (2017). Salmon provides fast and bias-aware quantification of transcript expression. Nat. Methods *14*, 417–419.

Pavlovic, J., Zürcher, T., Haller, O., and Staeheli, P. (1990). Resistance to influenza virus and vesicular stomatitis virus conferred by expression of human MxA protein. J. Virol. *64*, 3370–3375.

Peacock, T.P., Penrice-Randal, R., Hiscox, J.A., and Barclay, W.S. (2021). SARS-CoV-2 one year on: Evidence for ongoing viral adaptation. J. Gen. Virol. Published online April 15, 2021. https://doi.org/10.1099/jgv.0.001584.

Puray-Chavez, M., Tedbury, P.R., Huber, A.D., Ukah, O.B., Yapo, V., Liu, D., Ji, J., Wolf, J.J., Engelman, A.N., and Sarafianos, S.G. (2017). Multiplex single-cell visualization of nucleic acids and protein during HIV infection. Nat. Commun. *8*, 1882.

Qi, F., Qian, S., Zhang, S., and Zhang, Z. (2020). Single cell RNA sequencing of 13 human tissues identify cell types and receptors of human coronaviruses. Biochem. Biophys. Res. Commun. *526*, 135–140.

Richardson, P., Griffin, I., Tucker, C., Smith, D., Oechsle, O., Phelan, A., Rawling, M., Savory, E., and Stebbing, J. (2020). Baricitinib as potential treatment for 2019-nCoV acute respiratory disease. Lancet *395*, e30–e31.

Rihn, S.J., Aziz, M.A., Stewart, D.G., Hughes, J., Turnbull, M.L., Varela, M., Sugrue, E., Herd, C.S., Stanifer, M., Sinkins, S.P., et al. (2019). TRIM69 inhibits vesicular stomatitis Indiana virus. J. Virol. *93*, e00951-19.

Ritchie, M.E., Phipson, B., Wu, D., Hu, Y., Law, C.W., Shi, W., and Smyth, G.K. (2015). limma powers differential expression analyses for RNA-sequencing and microarray studies. Nucleic Acids Res. *43*, e47.

Robinson, M.D., McCarthy, D.J., and Smyth, G.K. (2010). edgeR: A Bioconductor package for differential expression analysis of digital gene expression data. Bioinformatics *26*, 139–140.

Robinson-McCarthy, L.R., McCarthy, K.R., Raaben, M., Piccinotti, S., Nieuwenhuis, J., Stubbs, S.H., Bakkers, M.J.G., and Whelan, S.P.J. (2018). Reconstruction of the cell entry pathway of an extinct virus. PLoS Pathog. *14*, e1007123.

Rothenburg, S., and Brennan, G. (2020). Species-specific host-virus interactions: Implications for viral host range and virulence. Trends Microbiol. *28*, 46–56.

Rubinstein, S., Familletti, P.C., and Pestka, S. (1981). Convenient assay for interferons. J. Virol. *37*, 755–758.

Schaefer, I.M., Padera, R.F., Solomon, I.H., Kanjilal, S., Hammer, M.M., Hornick, J.L., and Sholl, L.M. (2020). In situ detection of SARS-CoV-2 in lungs and airways of patients with COVID-19. Mod. Pathol. *33*, 2104–2114.

Schmidt, F., Weisblum, Y., Muecksch, F., Hoffmann, H.H., Michailidis, E., Lorenzi, J.C.C., Mendoza, P., Rutkowska, M., Bednarski, E., Gaebler, C., et al. (2020). Measuring SARS-CoV-2 neutralizing antibody activity using pseudotyped and chimeric viruses. J. Exp. Med. *217*, e20201181.

Schoeman, D., and Fielding, B.C. (2019). Coronavirus envelope protein: Current knowledge. Virol. J. *16*, 69.

Schoggins, J.W. (2018). Recent advances in antiviral interferon-stimulated gene biology. F1000Res. *7*, 309.

Schubert, K., Karousis, E.D., Jomaa, A., Scaiola, A., Echeverria, B., Gurzeler, L.A., Leibundgut, M., Thiel, V., Mühlemann, O., and Ban, N. (2020). SARS-CoV-2 Nsp1 binds the ribosomal mRNA channel to inhibit translation. Nat. Struct. Mol. Biol. *27*, 959–966.

Schultze, B., Krempl, C., Ballesteros, M.L., Shaw, L., Schauer, R., Enjuanes, L., and Herrler, G. (1996). Transmissible gastroenteritis coronavirus, but not the related porcine respiratory coronavirus, has a sialic acid (N-glycolylneuraminic acid) binding activity. J. Virol. *70*, 5634–5637.

Shajahan, A., Archer-Hartmann, S., Supekar, N.T., Gleinich, A.S., Heiss, C., and Azadi, P. (2021). Comprehensive characterization of N- and O- glycosylation of SARS-CoV-2 human receptor angiotensin converting enzyme 2. Glycobiology *31*, 410–424.

Shang, J., Wan, Y., Luo, C., Ye, G., Geng, Q., Auerbach, A., and Li, F. (2020). Cell entry mechanisms of SARS-CoV-2. Proc. Natl. Acad. Sci. USA *117*, 11727–11734.

Shema Mugisha, C., Vuong, H.R., Puray-Chavez, M., Bailey, A.L., Fox, J.M., Chen, R.E., Wessel, A.W., Scott, J.M., Harastani, H.H., Boon, A.C.M., et al. (2020a). A simplified quantitative real-time PCR assay for monitoring SARS-CoV-2 growth in cell culture. mSphere *5*, e00658-20.

Shema Mugisha, C., Vuong, H.R., Puray-Chavez, M., and Kutluay, S.B. (2020b). A facile Q-RT-PCR assay for monitoring SARS-CoV-2 growth in cell culture. bioRxiv. https://doi.org/10.1101/2020.06.26.174698.

Soneson, C., Love, M.I., and Robinson, M.D. (2015). Differential analyses for RNA-seq: Transcript-level estimates improve gene-level inferences. F1000Res. *4*, 1521.

Stukalov, A., Girault, V., Grass, V., Bergant, V., Karayel, O., Urban, C., Haas, D.A., Huang, Y., Oubraham, L., Wang, A., et al. (2020). Multi-level proteomics reveals host-perturbation strategies of SARS-CoV-2 and SARS-CoV. bioRxiv. https://doi.org/10.1101/2020.06.17.156455.

Sungnak, W., Huang, N., Bécavin, C., Berg, M., Queen, R., Litvinukova, M., Talavera-López, C., Maatz, H., Reichart, D., Sampaziotis, F., et al.; HCA Lung Biological Network (2020). SARS-CoV-2 entry factors are highly expressed in nasal epithelial cells together with innate immune genes. Nat. Med. *26*, 681–687.

To, K.F., and Lo, A.W. (2004). Exploring the pathogenesis of severe acute respiratory syndrome (SARS): The tissue distribution of the coronavirus (SARS-CoV) and its putative receptor, angiotensin-converting enzyme 2 (ACE2). J. Pathol. *203*, 740–743.

Tortorici, M.A., Walls, A.C., Lang, Y., Wang, C., Li, Z., Koerhuis, D., Boons, G.J., Bosch, B.J., Rey, F.A., de Groot, R.J., and Veesler, D. (2019). Structural basis for human coronavirus attachment to sialic acid receptors. Nat. Struct. Mol. Biol. *26*, 481–489.

Tyanova, S., Temu, T., and Cox, J. (2016). The MaxQuant computational platform for mass spectrometry-based shotgun proteomics. Nat. Protoc. *11*, 2301–2319.

UniProt Consortium (2019). UniProt: A worldwide hub of protein knowledge. Nucleic Acids Res. *47* (*D1*), D506–D515.

Varga, Z., Flammer, A.J., Steiger, P., Haberecker, M., Andermatt, R., Zinkernagel, A.S., Mehra, M.R., Schuepbach, R.A., Ruschitzka, F., and Moch, H. (2020). Endothelial cell infection and endotheliitis in COVID-19. Lancet *395*, 1417–1418.

Vlasak, R., Luytjes, W., Spaan, W., and Palese, P. (1988). Human and bovine coronaviruses recognize sialic acid-containing receptors similar to those of influenza C viruses. Proc. Natl. Acad. Sci. USA *85*, 4526–4529.

Walls, A.C., Park, Y.J., Tortorici, M.A., Wall, A., McGuire, A.T., and Veesler, D. (2020). Structure, function, and antigenicity of the SARS-CoV-2 spike glycoprotein. Cell *181*, 281–292.e6.

Wang, S., Qiu, Z., Hou, Y., Deng, X., Xu, W., Zheng, T., Wu, P., Xie, S., Bian, W., Zhang, C., et al. (2021). AXL is a candidate receptor for SARS-CoV-2 that promotes infection of pulmonary and bronchial epithelial cells. Cell Res. *31*, 126–140.

Weisblum, Y., Schmidt, F., Zhang, F., DaSilva, J., Poston, D., Lorenzi, J.C., Muecksch, F., Rutkowska, M., Hoffmann, H.H., Michailidis, E., et al. (2020). Escape from neutralizing antibodies by SARS-CoV-2 spike protein variants. eLife *9*, e61312.

Wickramasinghe, I.N., de Vries, R.P., Gröne, A., de Haan, C.A., and Verheije, M.H. (2011). Binding of avian coronavirus spike proteins to host factors reflects virus tropism and pathogenicity. J. Virol. *85*, 8903–8912.

Wilkerson, M.D., and Hayes, D.N. (2010). ConsensusClusterPlus: A class discovery tool with confidence assessments and item tracking. Bioinformatics *26*, 1572–1573.

Wrapp, D., Wang, N., Corbett, K.S., Goldsmith, J.A., Hsieh, C.L., Abiona, O., Graham, B.S., and McLellan, J.S. (2020). Cryo-EM structure of the 2019-nCoV spike in the prefusion conformation. Science *367*, 1260–1263.

Wu, Z., and McGoogan, J.M. (2020). Characteristics of and important lessons from the coronavirus disease 2019 (COVID-19) outbreak in China: Summary of a report of 72 314 cases from the Chinese Center for Disease Control and Prevention. JAMA *323*, 1239–1242.

Wu, F., Zhao, S., Yu, B., Chen, Y.M., Wang, W., Song, Z.G., Hu, Y., Tao, Z.W., Tian, J.H., Pei, Y.Y., et al. (2020). A new coronavirus associated with human respiratory disease in China. Nature *579*, 265–269.

Xia, H., Cao, Z., Xie, X., Zhang, X., Chen, J.Y., Wang, H., Menachery, V.D., Rajsbaum, R., and Shi, P.Y. (2020). Evasion of type I interferon by SARS-CoV-2. Cell Rep. *33*, 108234.

Xiao, H., Xu, L.H., Yamada, Y., and Liu, D.X. (2008). Coronavirus spike protein inhibits host cell translation by interaction with eIF3f. PLoS ONE *3*, e1494.

Xie, X., Muruato, A., Lokugamage, K.G., Narayanan, K., Zhang, X., Zou, J., Liu, J., Schindewolf, C., Bopp, N.E., Aguilar, P.V., et al. (2020). An infectious cDNA clone of SARS-CoV-2. Cell Host Microbe *27*, 841–848.e3.

Yang, Q., Hughes, T.A., Kelkar, A., Yu, X., Cheng, K., Park, S., Huang, W.C., Lovell, J.F., and Neelamegham, S. (2020). Inhibition of SARS-CoV-2 viral entry upon blocking N- and O-glycan elaboration. eLife *9*, e61552.

Yin, X., Riva, L., Pu, Y., Martin-Sancho, L., Kanamune, J., Yamamoto, Y., Sakai, K., Gotoh, S., Miorin, L., De Jesus, P.D., et al. (2021). MDA5 governs the innate immune response to SARS-CoV-2 in lung epithelial cells. Cell Rep. *34*, 108628.

You, Y., Richer, E.J., Huang, T., and Brody, S.L. (2002). Growth and differentiation of mouse tracheal epithelial cells: Selection of a proliferative population. Am. J. Physiol. Lung Cell. Mol. Physiol. *283*, L1315–L1321.

Yu, G., Wang, L.G., Han, Y., and He, Q.Y. (2012). clusterProfiler: An R package for comparing biological themes among gene clusters. OMICS *16*, 284–287.

Yuan, S., Peng, L., Park, J.J., Hu, Y., Devarkar, S.C., Dong, M.B., Shen, Q., Wu, S., Chen, S., Lomakin, I.B., et al. (2020). Nonstructural protein 1 of SARS-CoV-2 is a potent pathogenicity factor redirecting host protein synthesis machinery toward viral RNA. Mol. Cell *80*, 1055–1066.e6.

Zecha, J., Lee, C.Y., Bayer, F.P., Meng, C., Grass, V., Zerweck, J., Schnatbaum, K., Michler, T., Pichlmair, A., Ludwig, C., and Kuster, B. (2020). Data, reagents, assays and merits of proteomics for SARS-CoV-2 research and testing. Mol. Cell. Proteomics *19*, 1503–1522.

Zhao, Y., Zhao, Z., Wang, Y., Zhou, Y., Ma, Y., and Zuo, W. (2020). Single-cell RNA expression profiling of ACE2, the receptor of SARS-CoV-2. Am. J. Respir. Crit. Care Med. *202*, 756–759.

Zhou, B., Liu, J., Wang, Q., Liu, X., Li, X., Li, P., Ma, Q., and Cao, C. (2008). The nucleocapsid protein of severe acute respiratory syndrome coronavirus inhibits cell cytokinesis and proliferation by interacting with translation elongation factor 1alpha. J. Virol. *82*, 6962–6971.

Zhou, P., Yang, X.L., Wang, X.G., Hu, B., Zhang, L., Zhang, W., Si, H.R., Zhu, Y., Li, B., Huang, C.L., et al. (2020). A pneumonia outbreak associated with a new coronavirus of probable bat origin. Nature *579*, 270–273.

Zost, S.J., Gilchuk, P., Case, J.B., Binshtein, E., Chen, R.E., Nkolola, J.P., Schäfer, A., Reidy, J.X., Trivette, A., Nargi, R.S., et al. (2020). Potently neutralizing and protective human antibodies against SARS-CoV-2. Nature *584*, 443–449.

Zou, X., Chen, K., Zou, J., Han, P., Hao, J., and Han, Z. (2020). Single-cell RNA-seq data analysis on the receptor ACE2 expression reveals the potential risk of different human organs vulnerable to 2019-nCoV infection. Front. Med. *14*, 185–192.

Zürcher, T., Pavlovic, J., and Staeheli, P. (1992). Mouse Mx2 protein inhibits vesicular stomatitis virus but not influenza virus. Virology *187*, 796–800.

STAR★METHODS

KEY RESOURCES TABLE

REAGENT or RESOURCE	SOURCE	IDENTIFIER
Antibodies		
SARS-CoV-2 nucleocapsid antibody	Sino Biological Inc.	Cat# 40588-T62; Various lots were used throughout RRID: N/A
Goat anti-rabbit secondary antibody Alexa Fluor 488-conjugated	Thermo Fisher Scientific	Cat# A32731; RRID:AB_2633280
Anti-ACE-2 antibody	R&D Systems Inc.	Cat#AF933; Lot#HOK0320061; RRID:AB_355722
β-actin antibody	Sigma	Cat#A5316; Lot# 059M4770V; RRID:AB_476743
Vinculin antibody	Santa Cruz	Cat#Sc-73614; Lot#H0417 ; RRID:AB_1131294
DC-SIGN+DC-SIGNR Antibody	R&D Systems Inc.	Cat# MAB1621; Lot# DZX0617061; RRID: AB_2074321
Anti-GFP antibody	Sigma Aldrich Inc.	Cat#11814460001; Lot#42903200; RRID: AB_390913
AAK1 antibody	Bethyl	Cat#A302-146A; Lot#1 ; RRID: AB_1720315
AP2M1 antibody	Abcam	Cat#ab75995; Lot#GR236320-14 ; RRID: AB_1309955
pAP2M1-T156 antibody	Cell Signaling	Cat#3843; Lot#1 ; RRID: AB_2056358
pSTAT1-Y701 antibody	Cell Signaling	Cat#9167; Lot#25 ; RRID: AB_561284
pSTAT1-S727 antibody	Cell Signaling	Cat#8826; Lot#1 ; RRID: AB_2773718
STAT1 antibody	Cell Signaling	Cat#14994; Lot#5 ; RRID: AB_2737027
MX1 antibody	Cell Signaling	Cat#37849; Lot#1 ; RRID: AB_2799122
IFIT1 antibody	Cell Signaling	Cat#14769; Lot# 1; RRID: AB_2783869
pIKKα/β-S176/180 antibody	Cell Signaling	Cat#2697; Lot#19 ; RRID: AB_2079382
IKKα antibody	Cell Signaling	Cat#11930; Lot#5 ; RRID: AB_2687618
IKKβ antibody	Cell Signaling	Cat#8943; Lot#3 ; RRID: AB_11024092
pNFKB p65-S536 antibody	Cell Signaling	Cat#3033; Lot#17 ; RRID: AB_331284
NFKB p65 antibody	Cell Signaling	Cat#8242; Lot#13 ; RRID: AB_10859369
IRDye 800CW Donkey anti-Rabbit secondary antibody	Li-Cor	Cat#92632213; RRID: AB_621848
IRDye 800CW Donkey anti-Goat secondary antibody	Li-Cor	Cat#92632214; RRID: AB_621846
IRDye 680RD Donkey anti-Mouse secondary antibody	Li-Cor	Catt# 92668072; RRID: AB_10953628
S neutralizing antibody 2B04 (RBD-mAb)	Laboratory of Ali Ellebedy (Washington University in St. Louis) (Alsoussi et al., 2020)	N/A
S neutralizing antibody 2H04 (RBD-mAb)	Laboratory of Ali Ellebedy (Washington University in St. Louis) (Alsoussi et al., 2020)	N/A
S neutralizing antibodies SARS2-02, SARS2-38, SARS2-71, SARS2-31 (RBD-mAb)	Laboratory of Michael S. Diamond (Washington University in St. Louis) (Liu et al., 2021)	N/A
NTD-S specific antibodies (SARS2-11, SARS2-57)	Laboratory of Michael S. Diamond (Washington University in St. Louis) (This paper)	N/A
Bacterial and virus strains		
SARS-CoV-2 strain 2019 n-CoV/USA_WA1/2020	Centers for Disease Control and Prevention (gift of Natalie Thornburg)	Accession number: MN985325

(*Continued on next page*)

Continued

REAGENT or RESOURCE	SOURCE	IDENTIFIER
VSV-GFP-SARS-CoV-2-S $_{\Delta 21}$	Laboratory of Sean Whelan (Washington University in St. Louis) (Case et al., 2020)	N/A
DH10B	Thermo Fisher Scientific	Cat # EC0113
Biological samples		
Patient-derived airway epithelial cells	Laboratory of Steve Brody/Amjad Horani (Washington University in St. Louis)	N/A
Chemicals, peptides, and recombinant proteins		
Bafilomycin A	Sigma	CAS# B1793
SGC-AAK1 inhibitor	R&D Systems	65285; CAS: 2247894-32-0
E64D	Sigma	CAS# 88321-09-9
Apilimod	Laboratory of Sean Whelan (Washington University in St. Louis)	N/A
Camostat mesylate	Tocris	CAS# 59721-29-8
ACE2-Fc peptide	Laboratory of Daved Fremont (Washington University in St. Louis) (Case et al., 2020)	N/A
Incucyte® NucLight Red	Sartorius	Cat#4625
Incucyte® NucLight Rapid Red	Sartorius	4717
Lipofectamine RNAiMAX Transfection Reagent	Invitrogen	13778150
Sequencing Grade Modified Trypsin	Promega	PR-V5113
200-mg tC18 SepPak cartridge	Waters Technologies	WAT054925
16% paraformaldehyde	Alfa Aesar	Cat #43368
Dimethyl Sulfoxide (DMSO)	Sigma	D8418-500 mL
Phosphate-Buffered Saline (PBS) without calcium and magnesium	Corning	Cat#21-040-CM
Roswell Park Memorial Institute (RPMI) 1640 1X with L-glutamine	Corning	Cat# 10-040-CM
HEPES buffer 1M	Corning	Cat#25060-CI
Fetal Bovine Serum (Seradigm Life Science)	VWR	Cat#97068-085
Fetal Bovine Serum	Sigma	Cat#19B416
Dulbecco's modified Eagle's medium – high glucose (DMEM)	Sigma	Cat#D6429
Dulbecco's modified Eagle's medium/Ham's F-12 50/50 Mix (DMEM/F-12)	Corning	Cat#10-092-CV
Eagle's Minimum Essential medium (MEM)	Corning	Cat# 10-009-CV
0.05% Trypsin 0.53 mM EDTA 1X	Corning	Cat# 25-051-CI
Minimum Essential Medium Eagle (MEM) 10X	Sigma	Cat# M0275
Crystal violet	Fisher Scientific	Cat#C581-100
Methyl cellulose	Sigma	Cat#M0512
Protease	RNAscope® Fluorescent Multiplex Reagent Kit	Cat #320850
4′,6′-diamino-2- phenylindole (DAPI)	RNAscope® Fluorescent Multiplex Reagent Kit	Cat #320850
Polyethylenimine (PEI)	Polysciences	Cat# 23966-2
TMT Labels	Thermo Fisher Scientific	PIA37725
Puromycin	InvivoGen	Cat # ant-pr-1
Heparinase I	R&D Systems	Cat#7897-GH-010 Lot#DCWP0220071
Heparinase II	R&D Systems	Cat#6336-GH-010 Lot#TIE0220101
Heparinase III	R&D Systems	Cat#6145-GH-010 Lot#TKD0219061

(*Continued on next page*)

Continued

REAGENT or RESOURCE	SOURCE	IDENTIFIER
Critical commercial assays		
RNA-clean and concentrator-5	Zymo Research	R1013
Trizol	Thermo Fisher Scientific	15596018
TaqMan RNA-to-CT 1-Step Kit	Applied Biosystems	4392938
PureLink RNA Mini Kit	Invitrogen	12183025
iScript gDNA Clear cDNA Synthesis Kit	Bio-Rad	1725035
PowerUP SYBR Green Master Mixt	Applied Biosystems	A25778
Truseq stranded mRNA sequencing kit	Illumina	20020594
Quantitative fluorometric peptide assay	Pierce	PI23290
GeneArt Genomic Cleavage Detection Kit	Invitrogen	A24372
Deposited data		
RNA-seq (infected H522 cells)	GEO	GEO: GSE163547
Proteomics	ProteomeXchange	PXD023754 Reviewer account details: Username: reviewer_pxd023754@ebi.ac.uk Password: b2aH27kS
RNA-seq (airway cell lines)	NCBI SRA (bioproject)	PRJNA523380 and PRJNA533478
MSigDB	PUBMED: 21546393	http://www.gsea-msigdb.org/gsea/msigdb/index.jsp
UniProtKB human proteome	UniProt	https://www.uniprot.org/proteomes/UP000005640
UniProtKB SARS-CoV-2 proteome	UniProt	https://www.uniprot.org/proteomes/UP000464024
CORUM	PUBMED: 30357367	https://mips.helmholtz-muenchen.de/corum/
BioGRID Multi-validated interactions	PUBMED: 33070389	https://downloads.thebiogrid.org/BioGRID/Release-Archive/BIOGRID-4.2.193/BIOGRID-MV-Physical-4.2.193.tab3.zip
BioGRID SARS-CoV-2 interactions	PUBMED: 33070389	https://downloads.thebiogrid.org/File/BioGRID/Release-Archive/BIOGRID-4.2.193/BIOGRID-PROJECT-covid19_coronavirus_project-4.2.193.zip
Experimental models: Cell lines		
African Green Monkey: Vero	ATCC	CCL-81
African Green Monkey: Vero E6	ATCC	CRL1586
Human: H522	ATCC	CRL-5810
Human: KYSE30	Laboratory of John Hayes (University of Tennessee Health Science Center)	N/A
Human: SCC25	Laboratory of John Hayes (University of Tennessee Health Science Center)	N/A
Human: A427	Laboratory of Bernard Weissman (University of North Carolina)	N/A
Human: Detroit562	ATCC	CCL-138
Human: H596	ATCC	HTB-178
Human: H1299	ATCC	CRL-5803
Human: HC827	ATCC	CRL-2868
Human: PC-9	Sigma	90071810
Human: OE21	Sigma	96062201
Human: HEK293t	ATCC	CRL-11268
Human: Calu-3	ATCC	HTB-55
Hamster: PgsA-745	ATCC	CRL-2242

(*Continued on next page*)

Continued

REAGENT or RESOURCE	SOURCE	IDENTIFIER
Oligonucleotides		
See Table S7 for oligo sequences		N/A
Recombinant DNA		
pLV-EF1a-IRES-puro	Addgene	Addgene #85132
pLentiCRISPRv2-ACE2	Genscript	Clone ID K33520
pLentiCRISPRv2-NRP1	Genscript	Clone ID 1 and 2
pCCNG/nLuc	(Schmidt et al., 2020)	N/A
pCMV-SARS-CoV-2 S	(Schmidt et al., 2020)	N/A
Software and algorithms		
Data analysis and figure generation code	This paper	https://github.com/GoldfarbLab/H522_paper_figures
FlowJo	FlowJo	https://www.flowjo.com/solutions/flowjo/downloads
Image Studio	Li-Cor	https://www.licor.com/bio/image-studio-lite/
The R Project for Statistical Computing	The R Foundation	http://www.r-project.org/index.html
MaxQuant v1.6.16	Tyanova et al., 2016	https://www.maxquant.org/
clusterProfiler	Yu et al., 2012	https://bioconductor.org/packages/release/bioc/html/clusterProfiler.html
EdgeR	Robinson et al., 2010	https://bioconductor.org/packages/release/bioc/html/edgeR.html
Limma	Ritchie et al., 2015	https://bioconductor.org/packages/release/bioc/html/limma.html
Salmon	Patro et al., 2017	https://combine-lab.github.io/salmon
Tximport	Soneson et al., 2015	https://bioconductor.org/packages/release/bioc/html/tximport.html
ConsensusClusterPlus	Wilkerson and Hayes, 2010	https://bioconductor.org/packages/release/bioc/html/ConsensusClusterPlus.html
Fgsea	http://biorxiv.org/lookup/doi/10.1101/060012	https://bioconductor.org/packages/release/bioc/html/fgsea.html
ImageJ	NIH (https://imagej.net/software/imagej)	N/A
Other		
ImmEdge hydrophobic barrier PAP pen	Vector Laboratories	Cat #H-4000
12 mm collagen-coated coverslips	NeuVitro	Cat #GG-12-Collagen

RESOURCE AVAILABILITY

Lead contact

Further information and requests for reagents and resources should be directed to and will be fulfilled by the Lead Contact, Sebla B. Kutluay (kutluay@wustl.edu).

Materials availability

All unique reagents generated in this study are available from the Lead Contact

Data and code availability

Raw RNA sequencing data are available on the GEO repository (GEO: GSE163547) and NCBI SRA (bioproject, PRJNA523380 and PRJNA533478) for the lung and head/neck cancer cell lines.

Raw proteomics data are available via ProteomeXchange with identifier PXD023754.

Reviewer account details:

Username: reviewer_pxd023754@ebi.ac.uk

Password: b2aH27kS

R scripts to process data and generate figures are available on GitHub:
https://github.com/GoldfarbLab/H522_paper_figures
A1ny additional information required to reanalyze the data reported in this paper is available from the lead contact upon request.

EXPERIMENTAL MODEL AND SUBJECT DETAILS

Viral strains

SARS-CoV-2 strain 2019-nCoV/USA-WA1/2020 was obtained from Centers for Disease Control and Prevention (a gift from Natalie Thornburg). SARS-CoV-2 was propagated in Vero CCL-81 cells (America Type Culture Collection (ATCC)-CCL-81) at an MOI of 0.01 grown in Dulbecco's Modified Eagle's Medium (DMEM, Sigma) supplemented with 10% Fetal Bovine Serum (FBS, VWR) and 10 mM HEPES buffer (Corning). After amplification, the virus was titered on Vero E6 cells (ATCC-CRL1586) by plaque assays and sequenced to confirm identity. E484D (100%) and R682W substitutions (10%–40%) were found in our virus stocks, but we did not observe selection of additional S mutations following growth in H522 cells. All experiments involving SARS-CoV-2 were performed in a biosafety level 3 laboratory.

VSV-GFP-SARS-CoV-2-S $_{\Delta 21}$ virus was used as previously described (Case et al., 2020). Briefly, the VSV-GFP-SARS-CoV-2-S $_{\Delta 21}$ virus was propagated in the MA104 cell line (ATCC-CRL-2378.1) cultured in Medium 199 (GIBCO) supplemented with 10% FBS, 1% penicillin–streptomycin and 20 mM HEPES pH 7.7. MA104 cells were infected at an MOI of 0.01 at 37°C. After 1 hour, the media was replaced with Medium 199 supplemented with 10% FBS and 1% penicillin–streptomycin and grown at 34°C. The viral supernatant was collected 48 hpi and cell debris was cleared by centrifugation for 7.5 mins at 1000 x g. VSV-GFP-SARS-CoV-2-S $_{\Delta 21}$-R685S mutant was isolated from WT stock. E484K-R685S was an escape mutant isolated from monoclonal antibody SARS2-55 using R685S virus. Monoclonal antibody SARS2-55 was generated and as previously described (Liu et al., 2021). Briefly, plaque assays were performed to isolate the VSV-SARS-CoV-2 escape mutant on Vero E6-TMPRSS2 cells with the mAb in the overlay. Escape clones were plaque-purified on Vero E6-TMPRSS2 cells in the presence of mAb, and plaques in agarose plugs were amplified on MA104 cells with the mAb present in the medium. Viral stocks were amplified on MA104 cells at an MOI of 0.01 in Medium 199 containing 2% FBS and 20 mM HEPES pH 7.7 (Millipore Sigma) at 34°C. Viral supernatants were harvested upon extensive cytopathic effect and clarified of cell debris by centrifugation at 1,000 x g for 5 min. Aliquots were maintained at −80°C. Viral RNA was extracted from VSV-SARS-CoV-2 mutant viruses using the RNeasy Mini kit (QIAGEN), and S was amplified using the OneStep RT-PCR Kit (QIAGEN). The mutations were identified by Sanger sequencing (GENEWIZ). HEK293T-ACE2 and H522 cells were infected at MOI of 1-20 with VSV-GFP-SARS-CoV-2-S $_{\Delta 21}$ (and variants) and analyzed by FACS at 6 hpi (for HEK293T) or 24 hpi (for H522) cells. All experiments involving VSV-GFP-SARS-CoV-2-S $_{\Delta 21}$ were done in a biosafety level 2 laboratory.

Cell culture

All cell lines were maintained in a humidified incubator at 37°C with 5% CO_2 unless otherwise indicated. Cell line identities were validated by short tandem repeat analysis (LabCorp, Genetica Cell Line Testing), and cultures were regularly tested for mycoplasma contamination using the MycoAlert mycoplasma detection kit (Lonza). HEK293T and Calu-3 (ATCC-HTB-55) cells were cultured in DMEM (Sigma) supplemented with 10% FBS (VWR). A monoclonal population of HEK293T cells stably expressing human ACE2 was generated following lentiviral transduction through standard procedures and using the pLV-EF1a-IRES-Puro-ACE2 construct detailed below. The Vero CCL81 and Vero E6 cells were cultured in DMEM supplemented with 10% FBS and 10 mM HEPES buffer. Vero E6-TMPRSS2 and MA104 were obtained from ATCC and cultured as previously described (Case et al., 2020). The KYSE30 and SCC25 cell lines were a kind gift from the John Hayes Lab (UTHSC). The A427 (kind gift from Bernard Weissman Lab (UNC)) and Detroit562 (ATCC-CCL-138) cell lines were cultured in Eagle's Minimum Essential Medium (EMEM, Corning) supplemented with 10% FBS (Sigma), 1% penicillin–streptomycin (Corning), and 2 mmol/L L-glutamine (GIBCO). The SCC25 cell line was cultured in DMEM:F12 (Corning) supplemented with 10% FBS (Sigma), 1% penicillin–streptomycin (Corning), and 400ng/ml hydrocortisone (Sigma). The H522 (ATCC-CRL-5810), H596 (ATCC HTB-178), H1299 (ATCC CRL-5803), HCC827 (ATCC CRL-2868), PC-9 (Sigma #90071810), KYSE30 (kind gift from Luke Chen (NCCU)), and OE21 (Sigma # 96062201) cell lines were cultured in RPMI-1640 (Corning) supplemented with 10% FBS (Sigma) and 1% penicillin–streptomycin (Corning). PgsA-745 (ATCC #CRL 2242) cells were cultured in DMEM/nutrient mixture F-12 Ham, supplemented with 10% FBS (VWR).

Human airway epithelial cells were isolated from surgical excess of tracheobronchial segments of lungs donated for transplantation as previously described and were exempt from regulation by US Department of Health and Human Services regulation 45 Code of Federal Regulations Part 46 (Horani et al., 2012). Age range of donors was 17-69 years (mean 33.3y) and 75% of the donors were male. Tracheobronchial cells were expanded in culture, seeded on supported membranes (Transwell; Corning, Inc.) and differentiated using ALI conditions as detailed before (Horani et al., 2018; You et al., 2002).

METHOD DETAILS

Cloning

The *Homo sapiens* angiotensin-converting enzyme 2 (ACE2) transcript variant 2 amino acid sequence (NCBI Reference Sequence: NM_021804.3) was reverse translated using the Sequence Manipulation Suite and codon optimized using Integrated DNA

Technologies' Codon Optimization Tool. This fragment was synthesized as a gene block (IDT), with 5′-TTTTCTTCCATTTCAGGTGT CGTGAGGATCC added to the 5′ end and 5′- TGAGAATTCCTCGAGGGCGGCCGCTCTAGAGTC added to the 3′ end. This product was then inserted into the pLV-EF1a-IRES-Puro vector (Addgene Plasmid #85132) that had been digested with EcoRI and BamHI using Gibson Assembly (NEB). The sequence of the resulting construct was confirmed by Sanger sequencing and propagated in Stbl3 *E. coli* cells (Life Technologies) at 30°C followed by MaxiPrep (QIAGEN).

CMV-SARS-CoV-2-S was a kind gift from the Bieniasz Lab (Schmidt et al., 2020) and was used to generate pseudotyped lentivirus for infection of H522 cells. The various spike mutations were generated using PCR mutagenesis and cloned into CMV-SARS-CoV-2-S digested with AgeI and SpeI using Gibson Assembly Master Mix (NEB, #E2611). Primers used for cloning are listed in Table S7.

Lentivirus production and transduction

ACE2-expressing H522 and primary basal airway epithelial cells were generated as follows. Recombinant lentivirus was produced in HEK293T cells using a vector that expresses ACE2 driven by EF1 and a cassette to confer puromycin resistance together with psPAX2 packaging (Addgene #12260) and VSV-G envelope plasmids (Addgene #12259) as described (Horani et al., 2013). H522 and basal epithelial cells were incubated with virus-containing medium for 24 h, expanded for 3 days, then selected in puromycin (2.5 μg/mL) for 3 days. Production of lentiviruses pseudotyped with SARS-CoV-2 S was explained before (Schmidt et al., 2020). In brief, HEK293T cells grown on 10-cm dishes were transfected with 7μg of PSPAX, 7 μg of packagable genome encoding a GFP reporter and 2.5μg of SARS-CoV-2 S expression plasmid using polyethylenimine (PolySciences). Cell culture supernatants were filtered and concentrated using Lenti-X reagent (Clontech). HEK293T-ACE2 cells and H522 cells were transduced with varying amounts of pseudoparticles (10 and 30 μL for HEK293T, 150 μL for H522) and analyzed by FACS at 2 days post-infection.

SARS-CoV-2 infections, plaque assays, and FACS

Prior to infection, cells were seeded at 70%–80% confluency. Infections were done by addition of virus inoculum in cell culture media supplemented with 2% FBS and intermittent rocking for 1 h. Virus inoculum was removed, cells washed twice with 1x phosphate-buffered saline (PBS) and plated in cell culture media containing 10% FBS. Infections were monitored by plaque assays and qRT-PCR in cell culture supernatants. For plaque assays, Vero E6 cells were challenged with 10-fold serial dilutions of virus-containing supernatant, incubated for 1 h at 37°C with intermittent rocking, followed by addition of 2% methylcellulose and 2X MEM containing 4% FBS. 3 days post infection cells were fixed using 4% paraformaldehyde (PFA) and stained with crystal violet solution. For plaque assays and focus forming assays (FFA) in H522 cells, 2% methylcellulose and 2X RPMI containing 10% FBS combination was used. For FACS, cells were detached then fixed with 4% PFA for 20 min at room temperature, followed by permeabilization using 0.5% Tween-20 in PBS for 10 min. Cells were blocked with 1% bovine serum albumin (BSA) and 10% FBS in 0.1% Tween-20 PBS (PBST) for 1 h prior to staining with a rabbit polyclonal anti SARS-CoV-2 nucleocapsid antibody (Sino Biological Inc. catalog # 40588-T62) diluted 1:500 and incubated overnight at 4°C. The following day, after washed cells were stained with an Alexa Fluor 488-conjugated goat anti-rabbit secondary antibody (Invitrogen) at 1:1000 dilution. FACS was performed using a BD LSR Fortessa flow cytometer and analyzed by FlowJo software. For FFA, attached cells were fixed, and stained as described for FACS, but for permeabilization 0.1% Triton X-100 was used, images were analyzed using biomolecular imager Typhoon and ImageJ software.

RNA extraction, qRT-PCR, and RNA-seq

Cell associated RNA was extracted by Zymo RNA-clean and concentrator-5 kit following lysis of infected cells in 1X lysis buffer (20 mM TrisHCl, 150 mM NaCl, 5 mM MgCl2, 1% Triton X-100, 1 mM DTT, 0.2 U/μL SuperaseIN RNase Inhibitor, 0.1% NP-40) and following the manufacturer's instructions, or by Trizol extraction (Thermo Fisher Scientific). Extracted RNA was either subjected to Q-RT-PCR analysis for viral RNAs, cellular RNA, or RNA-seq. Viral RNA in cell culture supernatants was quantitated as detailed before (Shema Mugisha et al., 2020b). In brief, 5 μL of supernatant was mixed with 5 μL of 2x lysis buffer (2% Triton X-100, 50mM KCl, 100mM TrisHCl pH7.4, 40% glycerol supplemented with 400u/mL of SuperaseIN (Life Technologies)), followed by addition of 90 μL of 1X core buffer (5 mM (NH4)2SO4, 20 mM KCl and 20 mM Tris–HCl pH 8.3). 10 μL of this sample was used in a TaqMan-based Q-RT-PCR assay using TaqMan RNA-to-CT 1-Step Kit (Applied Biosystems, #4392938), alongside with RNA standards, targeting SARS-CoV-2 N gene. The primers and probe sequences are as described before (Shema Mugisha et al., 2020b). To study the interferon (IFN) response, cellular RNA was reverse transcribed with High-Capacity cDNA Reverse Transcription kit (Thermo Fisher Scientific) followed by Q-RT-PCR analysis using PowerUp SYBR Green Master Mix (Applied Biosystems). RNA levels were quantified using the ΔC_T method with *18S rRNA* as the reference target. ISG-specific primers are listed in Table S7.

RNA from human lung and airway cell lines were extracted using the PureLink RNA Mini Kit (Invitrogen). RT-PCR was performed on 1μg of RNA using the iScript gDNA Clear cDNA Synthesis Kit (Bio-Rad) and analyzed by qPCR using PowerUp SYBR Green Master Mix (Applied Biosystems) on a QuanStudio 5 machine. RNA levels were quantified using the ΔC_T method with *RPL13a* as the reference target. Gene specific primers are listed in Table S7.

Samples were prepared for RNA-seq using the Truseq stranded mRNA kit (Illumina) and subjected to sequencing on a Next-seq platform (1x75bp) at the Center for Genome Sciences at Washington University.

Immunofluorescence, RNA-ISH, and transmission electron microscopy

SARS-CoV-2 RNA and N protein were visualized in infected cells according to the published multiplex immunofluorescent cell-based detection of DNA, RNA and Protein (MICDDRP) protocol (Puray-Chavez et al., 2017). H522 cells were plated on 1.5 mm collagen-treated coverslips (GG-12-1.5-Collagen, Neuvitro) placed in 24-well plates one day prior to infection. Cells were infected with SARS-CoV-2 as above and fixed with 4% PFA at various time points post infection. Following fixation, cells were dehydrated with ethanol and stored at −20°C. Prior to probing for vRNA, cells were rehydrated, incubated in 0.1% Tween in PBS for 10 min, and mounted on slides. Probing was performed using RNAScope probes and reagents (Advanced Cell Diagnostics.) Briefly, coverslips were treated with protease solution for 15 min in a humidified HybEZ oven (Advanced Cell Diagnostics) at 40°C. The coverslips were then washed with PBS and pre-designed anti-sense probes specific for SARS-CoV-2 positive strand S gene encoding the spike protein (RNAscope Probe-V-nCoV2019-S, cat# 848561) were applied and allowed to hybridize with the samples in a humidified HybEZ oven at 40°C for 2 hr. The probes were visualized by hybridizing with preamplifiers, amplifiers, and finally, a fluorescent label. First, pre-amplifier 1 (Amp 1-FL) was hybridized to its cognate probe for 30 min in a humidified HybEZ oven at 40°C. Samples were then subsequently incubated with Amp 2-FL, Amp 3-FL, and Amp 4A-FL for 15 min, 30 min, and 15 min respectively. Between adding amplifiers, the coverslips were washed with a proprietary wash buffer. After probing for vRNA, samples were immunostained for the viral N protein. Coverslips were incubated in 1% bovine serum albumin (BSA) and 10% FBS in PBS containing 0.1% Tween-20 (PBST) at room temperature for 1 h. Samples were then incubated in a primary rabbit polyclonal SARS-CoV-2 nucleocapsid (N) antibody (Sino Biological Inc., Cat # 40588-T62) at 4°C overnight. After washing in PBST, the samples were then incubated in a goat anti-rabbit fluorescent secondary antibody (Invitrogen Alexa Fluor Plus 680, Cat# A32734) at room temperature for 1 h. Nuclei were stained with DAPI diluted in PBS at room temperature for 5 min. Finally, coverslips were washed in PBST followed by PBS and then mounted on slides using Prolong Gold Antifade.

Images were taken using a Zeiss LSM 880 Airyscan confocal microscope equipped with a × 63/1.4 oil-immersion objective using the Airyscan super-resolution mode. Images were taken of the samples using either the × 63 or × 10 objective.

For ultrastructural analyses by transmission electron microscopy, samples were fixed in 2% paraformaldehyde/2.5% glutaraldehyde (Polysciences Inc., Warrington, PA) in 100 mM sodium cacodylate buffer, pH 7.2 for 1 h at room temperature. Samples were washed in sodium cacodylate buffer and postfixed in 1% osmium tetroxide (Polysciences Inc., Warrington, PA) for 1 h. Samples were then rinsed extensively in dH_2O prior to en bloc staining with 1% aqueous uranyl acetate (Ted Pella Inc., Redding, CA) for 1 h. After several rinses in dH_2O, samples were dehydrated in a graded series of ethanol and embedded in Eponate 12 resin (Ted Pella Inc., Redding, CA). Sections of 95 nm were cut with a Leica Ultracut UCT ultramicrotome (Leica Microsystems Inc., Bannockburn, IL), stained with uranyl acetate and lead citrate, and viewed on a JEOL 1200 EX transmission electron microscope (JEOL USA Inc., Peabody, MA) equipped with an AMT 8 megapixel digital camera and AMT Image Capture Engine V602 software (Advanced Microscopy Techniques, Woburn, MA).

Live cell imaging and quantification

VSV-SARS-CoV-2-$S_{\Delta 21}$ viral infection rates were imaged and quantified using the Incucyte® S3 Life Cell Analysis System. VeroE6, H522, and H522-ACE2 cells were labeled with Incucyte® NucLight Red (Sartorius #4625) to generate stable expression of the red nuclear marker. Basal airway epithelial cells (AEC) were labeled with Incucyte® NucLight Rapid Red (Sartorius #4717) at the time of infection. VSV-SARS-CoV-2-$S_{\Delta 21}$ was then added to cells and immediately placed in the Incucyte®. Phase and fluorescent images were taken every hour to track viral infection. Percentage of GFP positive cells was calculated by dividing green object count by red object count for each well. Normalized GFP Intensity was calculated by dividing green intensity by percent confluence.

Immunoblotting

Human cell lines were grown to 70% confluence and lysed in RIPA (10% glycerol, 50mM Tris-HCl pH 7.4, 150mM NaCl, 2mM EDTA, 0.1% SDS, 1% NP40, 0.2% sodium deoxycholate) containing protease and phosphatase inhibitors (Thermo Scientific). Proteins were separated by SDS-PAGE, transferred to a nitrocellulose membrane, blocked in 5% milk, and incubated with primary antibodies overnight at 4°C. Washed membranes were incubated for 45 min at room temperature in secondary antibody solution (LI-COR IRDye 680, 800; 1:10,000 in 5% milk), imaged on an Odyssey® CLx, and analyzed using Image Studio Software. Antibodies were used at the following dilutions: ACE2 (R&D Systems #AF933, 1:200), β-actin (Sigma #A5316, 1:5000), Vinculin (Santa Cruz #sc-73614, 1:2000), AAK1 (Bethyl #A302-146A, 1:1000), AP2M1 (Abcam #ab75995, 1:1000), pAP2M1-T156 (Cell Signaling #3843, 1:1000), SARS-CoV-2-N (Sino Biological #40588-T62, 1:500), pSTAT1-Y701 (Cell Signaling #9167, 1:1000), pSTAT1-S727 (Cell Signaling #8826, 1:1000), STAT1 (Cell Signaling #14994, 1:1000), MX1 (Cell Signaling #37849, 1:1000), IFIT1 (Cell Signaling #14769, 1:1000), pIKKα/β-S176/180 (Cell Signaling #2697, 1:1000), IKKα (Cell Signaling #11930, 1:1000), IKKβ (Cell Signaling #8943, 1:1000), pNFKB p65-S536 (Cell Signaling #3033, 1:1000), NFKB p65 (Cell Signaling #8242, 1:1000),

CRISPR KO

H522 cells were transduced with a pLentiCRISPRv2 derived vector targeting *ACE2* (Genscript). The sgRNA (GTACTGTAGATGGTGCTCAT) targets exon 3 of *ACE2* (CCDS14169). After transduction, cells were selected in 3 μg/mL puromycin. Editing efficiency in the polyclonal population was determined using the Genomic Cleavage Detection assay (Invitrogen #A24372) and following the manufacturers protocol. The region surrounding the cleavage site was amplified using ACE2_Screen-F and

ACE2_Screen-R with the sequences listed in Table S7. H522 ACE2 KO monoclonal populations were generated by limiting dilution in 96-well plates and confirmed by sanger sequencing using the above ACE2_Screen primers. Sanger sequencing of the edited loci revealed unique 5 bp deletions in Exon 3 of ACE2, resulting in a truncated ACE2 protein lacking the C-terminal 672 amino acids, which includes the intracellular domain, transmembrane domain, collectrin domain and 75% of the carboxypeptidase domain.

H522 NRP1 KO cells were generated following the above protocol. Two sgRNAs targeting exon 4 of NRP1 were used: GTCGTAGCGACAGAACATCC (monoclones 1 and 2) and CACTAGGTGTTGTGTAGTTC (monoclone 3). H522 NRP1 KO monoclonal populations were confirmed by sanger sequencing using NRP1_Screen primers listed in Table S7.

siRNA transfections

siRNAs were reverse-transfected and the catalog numbers for each siRNA are listed in Table S7. In brief, 2.5 pmoles of siRNAs for each target was complexed with 0.75 μL of RNAimax transfection reagent following manufacturer's recommendations and added in 24-well cell culture dishes. H522 cells were then seeded at $1x10^5$ cells/well. Transfected cells were infected 1-day post-transfection with SARS-CoV-2 virus, and RNA extracted 3 or 4 days later by Trizol and processed for Q-RT-PCR analysis.

Pharmacological, neutralizing antibody, and sera effects on SARS-CoV-2 infections

In experiments where the mechanism of viral entry was probed, cells were pretreated with compounds as indicated in figure legends. Following viral adsorption, cells were continually kept in the presence of compounds till harvesting of the cell-associated total RNA by Trizol extraction. In experiments where the effects of neutralizing and S-targeting antibodies, soluble ACE2-Fc, convalescent sera and sera from vaccinated patients were assessed, virus inoculum was first pre-treated with the indicated reagents and added on target cells as detailed in Figure Legends. Monoclonal antibodies against SARS-CoV-2 S used in this study (2B04, 2H04, SARS2-02, SARS2-38, SARS2-71, SARS2-31) were previously explained (Alsoussi et al., 2020; Liu et al., 2021). Generation and validation of NTD-specific anti-S antibodies (SARS2-11 and SARS2-57) are explained below. Antibodies were used in the following concentrations for assessment of the neutralization efficacy based on published data: 2B04 (0.5 μg/mL); 2H04 (2 μg/mL); SARS2-02 (38 μg/mL), SARS2-38 (29 μg/mL), SARS2-71 (41 μg/mL), SARS2-31 (112 μg/mL), SARS2-11 (277 μg/mL), SARS2-57 (54 μg/mL).

Monoclonal antibody generation

BALB/c mice were immunized with 10 μg of SARS-CoV-2 RBD adjuvanted with 50% AddaVax (InvivoGen), via intramuscular route (i.m.), followed by i.m. immunization two and four weeks later with SARS-CoV-2 spike protein (5 μg and 10 μg, respectively) supplemented with AddaVax. Mice received a final, non-adjuvanted boost of 25 μg of SARS-CoV-2 spike or RBD (12.5 μg intravenously and 12.5 μg interperitoneally) 3 days prior to fusion of splenocytes with P3X63.Ag.6.5.3 myeloma cells. Hybridomas producing antibodies that bound to SARS-CoV-2-infected permeabilized Vero CCL81 cells by flow cytometry and to SARS-CoV-2 recombinant S protein by direct ELISA were cloned by limiting dilution. mAb used for neutralization studies was purified commercially (Bio-X Cell) from hybridoma supernatants after adaptation for growth under serum-free conditions. ELISA studies were done using hybridoma culture supernatants.

NTD-binding ELISA

Wells of 96-well microtiter plates were coated with purified recombinant SARS-CoV-2 SNTD (kindly provided by P. McTamney, K. Ren and A. Barnes, Astra Zeneca) at 4°C overnight. Plates were blocked with 2% non-fat dry milk and 2% normal goat serum in DPBS containing 0.05% Tween-20 (DPBS-T) for 1 h. Hybridoma culture supernatants were diluted 1:5 in blocking buffer, added to the wells in duplicate, and incubated for 1 h at ambient temperature. The bound antibodies were detected using goat anti-mouse IgG antibody conjugated with horseradish peroxidase (Southern Biotech, cat# 1030-05, 1:5,000 dilution for the assay) and TMB substrate (Thermo Fisher Scientific). Color development was monitored, 1 N hydrochloric acid was added to stop the reaction and the absorbance was measured at 450 nm using a spectrophotometer (Biotek).

ACE2 binding inhibition analysis. The assay was performed as described previously (Zost et al., 2020). Briefly, wells of 384-well microtiter plates were coated with 1 μg/mL purified recombinant SARS-CoV-2 S6Pecto protein at 4°C overnight. Plates were blocked with 2% non-fat dry milk and 2% normal goat serum in DPBS-T for 1 h. Mouse hybridoma culture supernatants were diluted five-fold in blocking buffer, added to the wells (20 μL per well) in quadruplicate, and incubated for 1 h at ambient temperature. Recombinant human ACE2 with a C-terminal Flag tag peptide was added to wells at 2 μg/mL in a 5 μL per well volume (final 0.4 μg/mL concentration of human ACE2) without washing of the plates, and then incubated for 40 min at ambient temperature. Plates were washed and bound human ACE2 was detected using HRP-conjugated anti-Flag antibody (Sigma-Aldrich, cat. A8592, lot SLBV3799, 1:5,000 dilution) and TMB substrate. ACE2 binding without antibody served as a control for maximal binding. The signal obtained for binding of the human ACE2 in the presence of each dilution of tested culture supernatant was expressed as a percentage of the human ACE2 binding without antibody after subtracting the background signal.

Removal of heparan sulfates from cell surface

Removal of cell surface heparan sulfate by sodium chlorate treatment was performed as before (Robinson-McCarthy et al., 2018). In brief, H522 cells were passaged in sulfate-free Joklik modified minimal essential medium (M8028, Sigma-Aldrich, St. Louis, MO) with 20% FBS with or without 50mM sodium chlorate for two passages prior to seeding for infection. SARS-CoV-2 infections were

performed in the presence of sodium chlorate. We confirmed the ability of H522 cells supporting SARS-CoV-2 infection following switching cells back to regular RPMI media, arguing against clonal selection of a subpopulation of cells following sodium chlorate treatment. As an alternative, H522 cells were treated with a combination of heparinase I (5.8 μg/mL), II (11 μg/mL) and III (11.2 μg/mL). In brief, herparinases were reconstituted per manufacturer's recommendation and cells seeded in 24-well plates were treated with the enzymes in 200 μL media containing heparinases for 90 minutes at 37°C. Virus inoculum (MOI: 0.1 IU/cell) was added on top and incubated for 1h at 37°C for adsorption. Virus inoculum and heparinases were removed, wells washed with PBS and replaced with RPMI-10%FBS.

Whole-cell proteomics sample preparation

The whole cell protocol was generally followed as described before (Mertins et al., 2018). Briefly, H522 cells were grown to 80%–90% confluency in 10cm cell culture dishes and then infected with SARS-CoV-2 (MOI = 1 pfu/cell) for indicated time points. Cells were then lysed in urea lysis buffer containing 8 M urea, 75 mM NaCl, 50 mM Tris (pH 8.0), 1 mM EDTA, phosphatase and protease inhibitors. Samples were high speed cleared for 15 min at max speed and protein concentration was determined via BCA. 1mg of protein lysate was aliquoted, then reduced with 5mM DTT and alkylated with 15mM chloroacetamide. The sample was then diluted with 50 mM Tris-HCl (pH 8.0) to decrease the urea concentration to < 2 M. Lysyl endopeptidase (Wako Chemicals, 129-02541) was then added at a 1mAU to 50μg of protein and incubated at 30°C for 4 h. Trypsin (Promega, PR-V5113) was then added in an enzyme/substrate ratio of 1:49 (wt/wt) for overnight digestion at 30°C. The reaction was quenched by acidifying the mixture to a concentration of 1% formic acid. Peptides were desalted using a 200-mg tC18 SepPak cartridge (Waters Technologies, WAT054925) with a vacuum manifold (protocol followed exactly as described in Mertins et al. (2018)) and speedvac'd dry. The sample was then resuspended in 50 mM HEPES (pH 8.5). The peptide concentration was determined by a quantitative fluorometric peptide assay kit (Pierce, PI23290). TMT labeling protocol from Zecha J et al. was followed, except for labeling duration (Zecha et al., 2020). Briefly, 300μg of peptide was aliquoted for TMT labeling and brought to a total volume of 60μL. TMT labels (Thermo, PIA37725) were resuspended in anhydrous acetonitrile so that the concentration of each label is 20μg/ μL. 15 μL of label (300 μg) was added to the sample and incubated at 25°C for 6 h. A test mix for labeling efficiency and label abundance was analyzed by mass spectrometry prior to mixing the samples. Samples were mixed according to the ratio determined by the test mix. The mixed sample was then desalted using a 200-mg tC18 SepPak cartridge (Waters Technologies, WAT054925) with a vacuum manifold (protocol followed exactly as described in Mertins et al. (2018)), speedvac'd dry, and resuspended in HPLC compatible buffer. HPLC fractionation and fraction pooling was followed exactly as described in Mertins et al. (2018). Following fractionation, samples were pooled to 25 fractions, speedvac'd dry, and resuspended in mass spec compatible buffer. 5% of each fraction was then analyzed by mass spectrometry for global whole cell proteomics.

Mass spectrometry data acquisition

Trypsinized peptides were separated via reverse-phase nano-HPLC using an RSLCnano Ultimate 3000 (Thermo Fisher Scientific). The mobile phase consisted of water + 0.1% formic acid as buffer A and acetonitrile + 0.1% formic acid as buffer B. Peptides were loaded onto a μPAC™ Trapping column (PharmaFluidics) and separated on a 200 cm μPAC™ column (PharmaFluidics) operated at 30°C using a 110 min gradient from 2% to 30% buffer B, followed by a 10 min gradient from 30% to 45% buffer B, flowing at 300 nL/min. Mass spectrometry analysis was performed on an Orbitrap Eclipse (Thermo Fisher Scientific) operated in data-dependent acquisition mode and used real-time sequencing (RTS) to trigger MS3 scans. MS1 scans were acquired in the Orbitrap at 120k resolution, with a 100% normalized automated gain control (AGC) target, auto max injection time, and a 375-1800 m/z scan range. MS2 targets were filtered for $\geq$ 50% precursor fit MS2, $\geq$ 2e4 signal intensity, charges 2-6, with a dynamic exclusion of 60 s, and were accumulated using a 1.2 m/z quadrupole isolation window. MS2 scans were performed in the ion trap at a turbo scan rate following collision induced dissociation (CID) at 35% collision energy. MS2 scans used a 100% normalized AGC target and auto max injection time. MS3 scans were trigged upon peptide identification using RTS. For RTS, the UniProtKB/Swiss-Prot human sequence database including isoforms (downloaded Aug. 2019) was appended with the SARS-CoV-2 proteome from UniProtKB and common contaminants from MaxQuant (Tyanova et al., 2016; UniProt Consortium, 2019). RTS parameters were set to a tryptic digestion with one missed cleavage, static Carbamidoemthyl cysteine modification (+57.0215) and TMT10 (+229.1629) on lysines and N-termini, and a variable oxidized methionine modification (+15.9949) and a maximum of 2 variable modifications per peptide. FDR filtering and protein close-out were enabled with a maximum of 5 peptides per protein and maximum search time of 50ms. The RTS scoring thresholds were set to Xcorr = 2.0, dCN = 0.1, and precursor ppm = 10 for all charges. MS3 scans were performed on the 10 most intense MS2 fragment ions identified by RTS and isolated using Synchronous Precursor Selection. MS3 scans used a normalized AGC target of 300%, auto max injection time, 50k resolution, 55% higher-energy collision dissociation collision energy, and 2 m/z wide MS2 isolation window. Acquisition was performed with a 2.5 s cycle time.

Whole-cell proteomics raw data processing

Raw MS data files were processed by MaxQuant (version 1.6.16.0) with the same sequence database used for RTS during data acquisition. The following parameters were used: specific tryptic digestion with up to two missed cleavages, fixed carbamidomethyl modification, variable modifications for protein N-terminal acetylation, methionine oxidation, and asparagine deamidation, match between runs, and reporter ion MS3 quantification. Lot specific impurities were used for the TMT labels.

QUANTIFICATION AND STATISTICAL ANALYSIS

Statistical parameters and details for each experiment are reported in respective figure legends. Generally, experiments were repeated with at least three biological replicates, represented by n. Each plot includes points for individual biological replicates and mean ± SEM error bars unless otherwise specified.

GraphPad Prism 9 software was used for statistical analysis. Two-way ANOVA was performed to assess significance and post hoc comparisons were employed using the Dunnett or Tukey test to correct for multiple comparisons. For statistical analysis of viral RNA (copies/cell), the data was log transformed prior to performing two-way ANOVA. The R statistical programming language was used for data processing and figure generation.

RNA-seq data

In order to standardize RNA-seq data from 3 different protocols in Figures 1A and S1, one of which used single end 50 base reads, all reads were trimmed to 50 bp length with FASTX-Toolkit (v0.0.13) and only the reads of the first pair were considered to adjust varying read lengths and technology. Those trimmed reads were mapped to the GRCh38 genome, aided with the Gencode v35 annotation of the transcriptome with STAR (v2.7.0.f_0328). Gene expression was quantified with Salmon (v1.3.0) in alignment-based mode (Patro et al., 2017). The resulting counts were normalized to a fixed upper quartile.

Salmon v1.1.0 was used for quantification of H522 RNA-seq data (Figure 5). Salmon indexes were constructed for both hg38, Gencode v27; as well as Sars-CoV-2 based on reference genome NC_045512.2. The R tximport package was used for per gene aggregation of human transcripts based on quantification from Salmon, using Gencode v27 as well (Soneson et al., 2015). Relative expression SARS-CoV-2 RNA was expressed in terms of the log transformed ratio of total reads mapping to SARS-CoV-2 versus GRCh38. 95% confidence intervals were calculated based on the assumption of normally distributed error.

Principle component analysis was performed without low-expressed genes. Starting with gene level read count quantification from Salmon and tximport as above. Genes with more than 5 counts-per-million in at least 24/48 samples were selected as an initial pre-processing step. Data normalization was performed by using the trimmed mean of M-values methods as implemented in the calcNormFactors function from the edgeR package. Normalized read counts were converted to counts-per-million and log2 transformed (logCPM). Principle component analysis was performed with the R function prcomp with data centering.

Differential expression analysis was performed starting with gene level read count quantification from Salmon and tximport as above. Marginally detected genes (less than 5 counts-per-million in less than 8/48 samples) were removed, as an initial pre-processing step. Data normalization was performed by using the trimmed mean of M-values methods as implemented in the calcNormFactors function from the edgeR package (Robinson et al., 2010). Normalized read counts were converted to counts-per-million and log2 transformed (logCPM). Differential expression analysis was subsequently performed using the Limma R-packages functions voom and eBayes (Ritchie et al., 2015). Mock infection was compared pairwise with post-infection time points, using data aggregated from the two highest MOIs (0.25 and 1.0) which appeared to have indistinguishable levels of SARS-CoV-2 gene expression. Multiple comparison correction was then performed based on the per-gene p.values from the eBayes function using the R package fdrTool. Log_2 fold-change values (logFC) were utilized as estimated by the limma eBayes function.

Data from the two highest MOIs were used, as above, in order to cluster based on temporal gene expression changes. LogCPM values for replicate conditions were averaged. Data were then filtered for genes with both an adjusted p value of < 0.005 and an absolute logFC > 2 at some time point in the experiment.

Whole-cell proteomics data

Protein abundances were computed by summing TMT reporter intensities for all spectra from a protein group's razor and unique peptides. MS3 spectra were filtered to have $>$ 4e3 summed TMT reporter intensity and a non-missing value for the pooled bridge channel. Protein groups were filtered to have at least two unfiltered MS3 spectra in at least two of three replicate experiments. Missing values for protein abundances were imputed with the minimum protein intensity observed in the dataset. To correct for loading differences, protein abundances were normalized to have equal total abundance per TMT channel. To facilitate comparison between the three TMT-plexes, protein abundances were then divided by their corresponding pooled bridge abundance.

Differential expression was determined with the R Limma package. Moderated t-statistics were computed between the 96 mock and 96 hpi samples with default settings. Benjamini-Hochberg adjustment was used for multiple test correction. Significance filters of an adjusted p value < 0.05 and an absolute $\log_2$ fold-change $> \log_2(1.3)$ were used. The lower fold-change threshold was employed in order to capture proteins whose differential expression peaked at other time points.

Protein-protein interactions for human proteins were extracted from BioGRID's multi-validated dataset (downloaded Jan. 2021) (Oughtred et al., 2021). Interactions between human and SARS-CoV-2 proteins were extracted from BioGRID's COVID-19 Coronavirus Project dataset (downloaded Jan. 2021) and filtered for interactions passing multi-validated criteria. Protein complexes were downloaded from CORUM (Giurgiu et al., 2019). Complexes were extracted for further analysis if they contained $>$ 2 proteins and $>$ 50% of the proteins were differentially expressed.

Cluster analysis

RNA-seq LogCPM values and protein abundances values were each converted to per-gene z-scores. Consensus clustering was then performed with the R ConsensusClusterPlus package (Wilkerson and Hayes, 2010). The non-defaults settings used were: reps = 50, innerLinkage = ''complete,'' and finalLinkage = ''ward.D2.'' The optimal number of seven clusters was chosen by manual inspection of clustering quality for consensus matrices with k = 1-12.

Gene set enrichment analysis

Over-representation of biological gene sets in individual temporal gene clusters for RNA-seq and proteomics data were investigated using the R clusterProfiler package and enricher function (Yu et al., 2012). Gene sets were downloaded from the MSIG data bank via the msigdbr R-project package, including ''Hallmark,'' ''Reactome,'' ''GO:BP,'' and ''GO:CC.'' (Jassal et al., 2020; Liberzon et al., 2015; Liberzon et al., 2011). Gene sets were considered significantly enriched in a cluster if adjusted p values were < 0.05 for proteomics. ''Hallmark'' and ''Reactome'' gene sets were similarly queried in the RNA-seq data using clusterProfiler, with a cutoff for significance of adjusted p value < 0.1.

Gene set enrichment analysis was performed on RNA-seq logCPM values (Figure 5G). Genes were ranked according to signal to noise ratio as defined by the Broad Institute GSEA software - $(\mu_a - \mu_b)/(\sigma_a + \sigma_b)$. Where μ is average the logCPM of a given gene under one experimental condition and σ the related standard deviation. Gene set enrichment analysis was then performed with default settings using the R-project fgsea package. Test gene-sets were downloaded from the MSIG data bank via the msigdbr R-project package. Only gene sets significantly associated with temporal expression clusters (using enrichr) in RNA-seq or whole cell proteomics data were subject to GSEA. Gene sets with adjusted p values < 0.05 detected for at least one time point were considered significant.